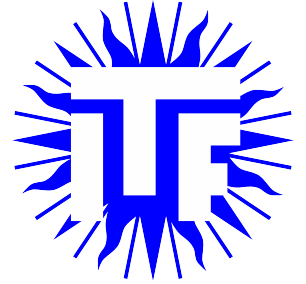**Universiteit Utrecht**

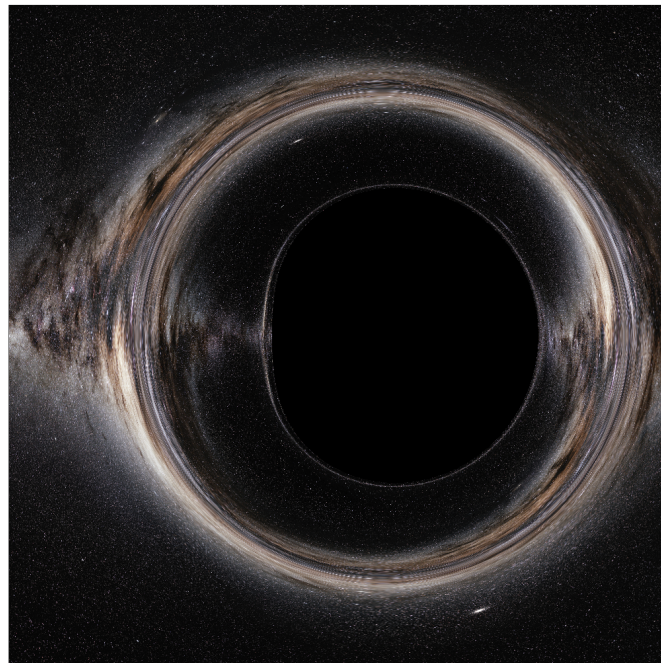# Faculteit Bètawetenschappen

Black holes and Symplectic Geometry

MASTER THESIS

Frank Imbens

Mathematics and Physics

Supervisors:

T. Hinderer SUPERVISOR
ITF, Utrecht University

A. del Pino Gomez SUPERVISOR
Mathematical Institute, Utrecht University
February 300 2023

Abstract

Black holes and other compact objects are powerful tools to observationally test Einsteins field equations. We explored the symplectic structure of the geodesics phase space of various solutions to Einsteins field equations in a vaccuum, using the tools provided by Riemannian geometry. The symplectic structure gives deeper insight into the geodesics around, and especially close to the black hole. This becomes a very difficult analytical problem for more complex spacetimes, and so we turned to numerical calculations. Using parallel processing on a graphical processing unit we created visual images of exotic compact objects, and explored the periodic orbits of light around these objects.

Contents

1 Introduction

Einsteins theory of relativity has revolutionized the way we view gravity. Rather than seeing gravity as a force it posits gravity as a curvature in space and time, bending paths of particles not by force, but by changing what a straight line is. This theory was first observationally checked by the perihelion precession of the planet Mercury, a movement that was at first thought to be caused by another planet.

The theory also gave rise to some strange objects that were more unexpected than small variations in the orbits of planets. The most well known of these is the black hole as discovered by Schwarzschild in 1916 [Sch16]. This object consisted of a singularity in spacetime, shrouded in an event horizon. This event horizon marks the border in space where the pull of the singularity becomes so strong that time itself points inwards to the singularity, meaning not even light can escape. After this more solutions of this type were discovered. Descriptions of a spinning black hole were made by Kerr. This spinning black hole, besides just pulling space in towards itself also twists space, dragging it along with the rotation. This so-called frame drag acts on test particles in much the way a spinning whirlpool would on a ship, allowing it to orbit much closer along with the rotation than against it. Furthermore it's internal structure changes significantly. It has an inner and an outer event horizon, and it has a circular singularity rather than a point singularity. Black holes such as these are defined by only their mass, charge and spin, and the no-hair theorem conjectures that these are the only possible characteristics a black hole can have. However more solutions were discovered that contradict this idea. One such solution is the Manko-Novikov spacetime, this is an extension to the Kerr spacetime adding extra multipole moments of rotation. This solution is often considered non-physical due to some of it's internal characteristics. Objects such as black holes could never exist in the Newtonian model for gravity, and thus their existence can be seen as a test of relativity.

With the advent of technologies like gravitational wave detection and better telescopes we have started being able to observe the effects of these compact objects. It was only in 1998 that the first proof of a black hole in the centre of our galaxy was found [Ghe+98]. Rather than directly observing the black hole this was done using infrared telescopes to observe the orbits of stars around the black hole. It was only in 2019 that the first visual images of what we believe to be a black hole were made by the Event Horizon Telescope [al19]. This black hole is the supermassive black hole at the center of Messier 87. More recently the EHT collaboration also created visual images of the black hole at the centre of our own galaxy. It is clear that these images can be powerful tools to test relativity when compared to simulations of shadows, the M87 black hole shadow was used to compute the mass of the black hole in [Aki+19]. Many others also used these images as an opportunity to compare to simulated shadows of various alternative black holes, such as [GA23].

To be able to theoretically describe such objects, we will need to delve into differential geometry. This is the theory of manifolds, and the structure on those manifolds. The manifold structure that describes the spacetimes of relativity is given by pseudo-Riemannian geometry. Riemannian geometry was first created to be able to give a local concept of distance to manifolds. This concept of distance is given in the form of a smooth family of inner products on the tangent space. This concept of distance was connected by Levi Civita [Lev16] to that of parallel transport and covariant derivatives. However the structure of pure Riemannian metrics is too rigid the describe the manifolds of general relativity, so we turn to pseudo-Riemannian manifolds.

A pseudo-Riemannian manifold is given by a manifold Q and a metric g. This metric is a symmetric and non-degenerate 2-tensor $g : TQ \times TQ \to \mathbb{R}$. In the case that g is positive definite it forms a smooth family of inner products on TQ, and the manifold is called Riemannian. This will however not be the case for the manifolds we find in general relativity. Here the metrics are Lorentzian, which means that locally they have one negative direction and three positive ones. The canonical example of this is $\mathbb{R}^4$ with the Minkovski metric $\eta = \text{diag}(-1, 1, 1, 1)$. This is often called flat space, and is the subject of study in the special theory of relativity.

We can see that this metric splits vectors or directions into three distinct sets. Those vectors that have $g(v, v) < 0$ are called timelike, and these directions are those that particles and objects with mass can travel. Directions with $g(v, v) = 0$ are called lightlike, these are the directions that light can travel, and form the lightcone. Lastly directions with $g(v, v) > 0$ are spacelike, these paths cannot be followed by physical objects. This splitting gives rise to the lightcone, which is defined by the points reached by light- and timelike directions from some starting points. This gives all the points in the causal future of our starting point, which is all the points that can be reached and affected. In the flat case this lightcone starting at a point looks like

a cone, where light travels diagonally at a 45 degree angle to the time coordinate, in a straight line.

Once the space becomes more complicated it helps to look not just at the spacetime manifold, but at the entire phase space. First one can do this by going from the spacetime manifold Q to it's tangent space TQ. A point in this space encodes not just a position but a velocity. Now one can define a Lagrangian, which is a function $\mathcal{L} : TQ \to \mathbb{R}$. On a pseudo-Riemannian manifold this Lagrangian is often given by $\mathcal{L}(q, v) = g_q(v, v)$, the dynamics can be extracted from this Lagrangian using the Euler-Lagrange equations which follow from calculus of variations.

However it is often simpler to move from a Lagrangian description to a Hamiltonian description. In this case we have not the tangent space but the cotangent space T^*Q as our phase-space, and a Hamiltonian $H : T^*Q \to \mathbb{R}$. The reason we go to the cotangent space is because it allows a canonical symplectic structure. A symplectic structure on a manifold M is a 2-form ω which is closed, non-degenerate and anti-symmetric. This symplectic form allows us to extract dynamics from the Hamiltonian by the definition $dH = \omega(X_H, \cdot)$. A deep treatment of all the geometric properties of symplectic spaces can be found in [D M98], which includes many theorems on symmetries of systems, such as Noethers theorem and Marsden-Weinstein quotients. These theorems form powerful tools to simplify our system of geodesics. Noethers theorem can be used to find symmetries and conserved quantities of the system, allowing for qualitative analysis. Marsden-Weinsteins theorem extends on this by allowing a reduction of the dimension of the system, to both simplify calculations and allow for easier intuition into the dynamics.

Sadly analytical calculations become very hard for more complicated spacetimes such as rotating black holes. For this we turn to numerically solving the geodesic equation. The standard way of solving differential equations is using numerical integrators. The simplest of these is Eulers method, which is first order. This means that every timestep is defined only by the first derivative. It is clear that as the timestep h gets smaller, this more precisely models the function, where the error is of the order $O(h^2)$. We can however do better, Runge-Kutta integration schemes can get an error of $O(h^n)$ with as high an order as one wants, but in general the best compromise between speed and precision is found at order 4, with an error of $O(h^5)$. We could also look at symplectic integrators, these are special types of integrators that are built so they conserve static quantities. For instance in the case of a Hamiltonian equation they conserve the levelset of the Hamiltonian exactly, where Eulers method, or Runge-Kutta schemes would drift. Sadly in our case these schemes remain implicit, which while not making them unusable, significantly limits their execution speed.

We want to use these numerical calculations to create visual images of the black hole. To do this we have to generate a large surface with initial conditions which will form our perspective. After this we propagate these as lightlike geodesics, colouring the pixel they represent on the screen a different colour based on the final position after propagation. While modern processor hardware has come a long way in parallel processing, allowing us to propagate upwards of 10 rays at the same time, this pales in comparison to using Graphical processors. These are made specifically for the kind of task of doing the same calculations thousands of times in parallel, with slightly varying inital conditions. We will be using such hardware to be able to create visual results of black holes at a resolution not easily acquired on a home computer before.

Using a similar technique, but with a different set on inputs we can also look at periodic orbits around a black hole, specifically periodic orbits of light. This can be done by starting the orbits near an expected periodic orbit and seeing how far they diverge from their starting positions. These orbits often correlate with the edge of the shadow. Furthermore from a mathematical perspective the periodic orbits of Hamiltonian systems are of great interest.

In this work we will first be describing the mathematical theorems we use. After that we will apply this to the Schwarzschild spacetime. We will derive for this black hole both what the shadow should look like, and what periodic orbits light can follow. After this we will compare this to a numerical analysis, which we will then expand to Kerr and Manko-Novikov spacetimes. Shadows of Manko-Novikov spacetimes were simulated before in [M W18], we hope to significantly increase the resolution of these simulations, while using simpler computational techniques that are more easily expanded to other spacetimes. We will also compare the structure visible in the shadow to analysis of periodic orbits, as these will often correlate with the boundary of the shadow.

2 Symplectic Geometry

In this chapter we will define the groundworks of symplectic geometry, which will be the structure on which we base the dynamics of the physical systems we define later. The structure will take the form of an anti-symmetric 2-form on a manifold.

2.1 Differential Geometry

To start we will define some of the standard notations and objects in geometry, upon which we will build our knowledge of symplectic and Riemannian geometry. These two geometrical structures will form the mathematical foundation for our physical calculations. Basic knowledge of manifolds and (co)-tangent spaces is assumed, a much more extensive explanation of all these can be found in [Lee13]. We use results from both the fields of general relativity in physics, and geometry in mathematics. These fields use very different notations, which provide better insight into different situations. Because of this we include a quick explanation of the index notation as compared to the notation often used in geometry.

Definition 2.1.1. Given a manifold M with a vectorfield $X \in TM$ and a chart $\chi : \mathbb{R} \supset U \to M$ we define:

$$X^\mu = \chi^* X \in T\mathbb{R}^n \tag{1}$$

Similarly for a 1-form $\alpha \in T^*M$ we define

$$\alpha_\mu = \chi^* \alpha \in T^*\mathbb{R}^n \tag{2}$$

Important to note is that a lower index means a 1-form and a higher index means a vector. Multiple indices of different types give a tensor, for example:

$$Y^\nu_\mu = \chi^* Y \in (T^*M \otimes TM)^* \tag{3}$$

Note that the chart is noted implicitly, as in this notation we often only consider a single chart whose image covers the part of the manifold we are interested in.
For derivatives this works analogously, we write

$$\partial_\mu f = \chi^* df \tag{4}$$
$$X^\mu \partial_\mu f = \chi^* \mathcal{L}_X f \tag{5}$$

It is important to note that often charts are used that do not cover the entire manifold, for example polar coordinates can be used to describe the plane minus the origin. So all use of this index notation is local.

2.2 Symplectic structures

For our treatment of symplectic manifolds we follow the lecture notes by Fabian Ziltener [Zil21]. The symplectic structure is encoded in the symplectic form, which we define as follows:

Definition 2.2.1. Given a manifold M, we call a 2-form ω on M *symplectic* if it is anti-symmetric, closed and non degenerate. The anti-symmetric property means that at any $x \in M$, for $v, w \in T_xM$ we have $\omega_x(v, w) = -\omega_x(w, v)$. Closedness means that $d\omega = 0$. Lastly non-degenerateness means that at a point $p \in M$ we have no $v \in T_pM$ such that $\iota_v\omega_p = \omega(v, \cdot) = 0$. This leads us to define the map

$$\omega^\flat : TM \to T^*M \tag{6}$$
$$v \mapsto \iota_v\omega \tag{7}$$

The non-degenerateness property now is equivalent to this map being of maximal rank and thus inverteble. We call the inverse $\omega^\sharp$.

2.3 Hamiltonian mechanics

Symplectic geometry found its roots in classical mechanics in physics. It was used to rigorously define the concept of a Hamiltonian and its dynamics.

Definition 2.3.1. In symplectic geometry a Hamiltonian is given by a function $H : M \to \mathbb{R}$. Its dynamics are given by a vectorfield $X_H \in TM$ defined implicitly by

$$dH = \iota_{X_H}\omega \tag{8}$$

Or, using the fact that ω is non-degenerate and thus $\omega^\flat$ can be inverted, we can define it explicitly by

$$X_H = \omega^\sharp(dH) \tag{9}$$

The fact that this X_H always exists and is unique now follows immediately from existence of $\omega^\sharp$.

The reasons we are interested in such vectorfields is that their dynamics correspond to physical dynamics, and the manifold gives the phase space. However before we get to the physics we will show a few useful properties of this vectorfield. Firstly we show that the Hamiltonian itself is constant under its dynamics.

Proposition 2.3.2. *The flow of X_H preserves H and ω*

Proof. We note that:

$$X_H(H) = dH(X_H) \tag{10}$$
$$= \omega(X_H, X_H) \tag{11}$$
$$= 0 \tag{12}$$

As ω is anti-symmetric. We note also that

$$\mathcal{L}_{X_H}(\omega) = d\iota_{X_H}\omega + \iota_{X_H}d\omega \tag{13}$$
$$= ddH + \iota_{X_H}0 \tag{14}$$
$$= 0 \tag{15}$$

Here we used Cartan's formula $\mathcal{L}_X = d\iota_X + \iota_X d$ ∎

In physics the Hamiltonian often gives the energy of the system at a certain point in phase space. In this case the above proposition is equivalent to conservation of energy.
Next we will show that given a codimension 1 submanifold $S \subset M$ it has well defined dynamics up to parametrization, which agree with those given by any Hamiltonian H of which S is a levelset.

Proposition 2.3.3. *Take a symplectic manifold (M, ω), a Hamiltonian $H : M \to \mathbb{R}$ and codimension 1 submanifold S that is a regular level set of H. Then X_H spans the 1-dimensional kernel of ω restricted to TS.*

Proof. Take a point $p \in S$, we show that if we restrict ω to T_pS we get an at most 1-dimensional kernel

$$\left\{ v \in T_pS \mid \iota_v\omega_p|_{T_pS} = 0 \right\}$$

We take $\omega^\flat(T_pS)$, this is a codimension 1 hypersurface in T_p^*M. We note that $\{\alpha \in T_p^*M | \alpha(T_pS) = 0\}$ is 1 dimensional as T_pS is codimension 1. So the dimension of the kernel of ω on T_pS is at most 1. We also know that it must be at least 1, as if it had a trivial kernel S would be a symplectic manifold of odd dimension, which is impossible.
Next we show this kernel is spanned by X_H. We see that $T_pS = \ker(dH) \subset T_pM$ So for every $v \in T_pS$ we have

$$\omega_p(X_{H,p}, v) = dH(v) \tag{16}$$
$$= 0 \tag{17}$$

This means for any Hamiltonian the dynamics of its vector field are defined by the levelsets, up to some local scaling. ∎

Lemma 2.3.4. *Take a symplectic manifold (M, ω), a Hamiltonian $H : M \to \mathbb{R}$ and a non-zero function $f : M \to \mathbb{R}$. H and fH have the same dynamics on the levelset $H = 0$ as long as it is regular.*

Proof. Since $f \neq 0$ we can state that $H_0 = \{x \in M | H(x) = 0\}$ is equal to $\{x \in M | f(x)H(x) = 0\}$. So, since it is a regular levelset both of the Hamiltonian H and fH, the dynamics are equal up to parametrisation by proposition 2.3.3. $\qquad\square$

Sadly we lose the nice structure of being a symplectic manifold on S, but in some cases we regain a new structure. This new structure is called a contact structure, an equally deep theory as that of symplectic geometry. Here too we will not take many deep dives into this theory, as in our physical problems only very simple contact manifolds will appear.

2.4 The Canonical Symplectic Structure

An important example of a symplectic structure is the canonical symplectic structure on T^*Q for a given manifold Q. We first define the Liouville form λ on T^*Q at a given point x. We take $q : T^*Q \to Q$ the standard projection, and define $\lambda = p \circ dq$, where $p \in T^*_{q(x)}Q$ is the element such that $x = (p, q)$. By slight abuse of notation we will usually write $x = (p, q)$ as local coordinates in which T^*Q is equivalent to $\mathbb{R}^n \times \mathbb{R}^n$ where the first component corresponds to the cotangent fibre.
We now define $\omega = -d\lambda$. It is immediately clear that this form is indeed anti-symmetric and closed by the definition of the external derivative d. For non-degenerateness we will refer simply to our coordinates p and q, as we see in those local coordinates $\omega = dq \wedge dp$, which is clearly non-degenerate.
In the physics picture, specifically in general relativity, we take Q to be our spacetime manifold, which will later be equipped with a pseudo-Riemannian metric. Then T^*Q becomes the phase space. In local coordinates we call q the position and p the momentum.

2.5 Symplectic reduction and Noether

Often in physics we have systems with high degrees of symmetry. Such symmetry can be useful to reduce the dimension of a problem to make its dynamics both more intuitive and easier to simulate. We will not give the full proof of this theorem, however we will give a short proof of Noethers theorem, meant to give an intuitive understanding of how the physics is described by the mathematics. We will follow the lecture notes by Fabian Ziltener again here. To understand the meaning of both theorems we will first need some groundwork. Suppose we have a Lie group G acting on a symplectic manifold M by symplectomorphisms. We call such an action Hamiltonian if we can make a moment map:

Definition 2.5.1. Moment map: Given a group action of G on M by symplectomorphisms a moment map is a map $\mu : M \to \mathfrak{g}^*$ from the manifold to the dual of the Lie algebra of G. This map has the following two properties:

$$d\langle \mu, \xi \rangle = \omega(X_\xi, \cdot) \tag{18}$$
$$\mu(gx) = Ad^*(g)(\mu(x)) \tag{19}$$

Next we will show some properties of transformations that will help us show Noethers theorem for our specific purposes.

Lemma 2.5.2. *A lift of a local diffeomorphism $f : Q \to Q'$ to cotangent spaces preserves λ. We say f is exact. [Zil21]*

Proof. Suppose we have a map $f : Q \to Q'$ that is a local diffeomorphism. We define

$$f_* : T^*Q \to T^*Q' \tag{20}$$

as

$$f_*(q, p) = (f(q), p \circ df^{-1}) \tag{21}$$

Then

$$(f_*)^*(\lambda'_{can}) = \lambda_{can} \tag{22}$$

As we see:

$$(f_*)^*(\lambda'_{can}) = \lambda'_{can} \circ d(f_*) \tag{23}$$
$$= p' \circ dq' \circ d(f_*) \tag{24}$$
$$= p \circ df^{-1} d(q \circ f_*) \tag{25}$$
$$= p \circ dq \tag{26}$$
$$= \lambda_{can} \tag{27}$$

This means the action is exact. This concludes the proof. □

Lemma 2.5.3. *An exact action is Hamiltonian. [Zil21]*

Proof. Let M a manifold and let G act on M. Let λ a 1-form on M such that $\omega = -d\lambda$ and let $\mu : M \to \mathfrak{g}^*$ defined by $\mu(x)(\xi) = \iota_\xi \lambda = \lambda(\xi_m)$. Because the action is exact we know $g^*\lambda = \lambda$ for all $g \in G$. So:

$$\mathcal{L}_{X_\xi} = \iota_{X_\xi} d\lambda + d\lambda(X_\xi) \tag{28}$$
$$\iota_{X_\xi}\omega = d\lambda(X_\xi) \tag{29}$$
$$\iota_{X_\xi}\omega = d\langle\mu, \xi\rangle \tag{30}$$

and

$$\mu(gx)(\xi) = \lambda_{gx}(X_\xi(gx)) \tag{31}$$
$$= g^*\lambda(X_{Ad(g)(\xi)}) \tag{32}$$
$$= Ad^*(g)(\mu(x))(\xi) \tag{33}$$

Then μ is a momentum map and thus the G action on M is Hamiltonian. □

Lemma 2.5.4. *An action of G on a manifold Q lifts to a Hamiltonian action on T^*Q. [Zil21]*

Proof. Since the action G acts by diffeomorphisms we can apply lemma 2.5.2 and then lemma 2.5.3 to gain that the lifted action is indeed Hamiltonian. □

Before we prove Noethers theorem, we will give an insightful and much simpler proof, assuming our action has only one dimension. In that case, the symmetry can be generated by a single vectorfield X on Q which extends to a Hamiltonian vectorfield on $T*Q$, the Hamiltonian of this vectorfield is given exactly by the conserved momentum, which is the 'dual' of X as generated via λ. And furthermore the fact that one Hamiltonian is invariant under the other is immediately seen from the fact that ω is anti-symmetric, so as

$$0 = dH_1(X_{H_2}) \tag{34}$$
$$= \omega(X_{H_1}, X_{H_2}) \tag{35}$$
$$= -\omega(X_{H_2}, X_{H_1}) \tag{36}$$
$$= -dH_2(X_{H_1}) = 0 \tag{37}$$

We will now show the full statement for an action with a higher dimension.

Lemma 2.5.5. Noethers theorem: *given a Hamiltonian H on M and a Hamiltonian action G on M that preserves H. Then the momentum map μ of G is invariant under the dynamics of X_H.*

Proof. We will show that $\langle\mu, \xi\rangle \circ \phi_H = \langle\mu, \xi\rangle$ for any fixed ξ. We take $X_{\langle\mu,\xi\rangle}$ to be the Hamiltonian vector field generated by this function. We note that this vector field is equal to X_ξ, as

$$\omega(X_{\langle\mu,\xi\rangle}, \cdot) = d\langle\mu, \xi\rangle = \omega(X_\xi, \cdot) \tag{38}$$

by the definition of the momentum map and non-degeneracy of ω.
Next we note that

$$H\big(\exp(t\xi(p,q))\big) = H(p,q) \tag{39}$$

and by taking a derivative:

$$0 = dH(X_\xi) \tag{40}$$
$$= dH(X_{\langle\mu,\xi\rangle}) \tag{41}$$
$$= \omega(X_H, X_{\langle\mu,\xi\rangle}) \tag{42}$$
$$= d(\langle\mu,\xi\rangle)(X_H) \tag{43}$$

From this it follows that $\langle\mu,\xi\rangle$ is constant under the movement of H. And as such so is μ. $\qquad\square$

From a physical perspective Noethers' theorem is very powerful. Conserved momenta give a lot of information about a system, and their preservation form good sanity checks in simulations.
Much stronger than simply conserved variables, the Marsden-Weinstein-Meyer theorem states that one can actually reduce the dimension of the problem. This is an incredibly powerful tool in both mathematics and physics.

Theorem 2.5.6. *Let (M,ω,G,μ) a Hamiltonian G-space for a compact Lie group G. Let $i : \mu^{-1}(0) \to M$ the inclusion map. Assume that G acts freely on $\mu^{-1}(0)$. Then the following holds:*

1. *The orbit space $\mu^{-1}(0)/G$ is a manifold*

2. *$\pi : \mu^{-1}(0) \to \mu^{-1}(0)/G$ is a principal G bundle*

3. *There is a symplectic form ω' on $\mu^{-1}(0)$ satisfying $i^*\omega = \pi^*\omega'$*

We will not prove this entire theorem here, as it is an extensive proof that other sources have detailed explanations of. [Zil21] There are also also stronger versions of this theorem, applying to other coadjoint orbits in $\mathfrak{g}^*$ than 0:

Theorem 2.5.7. *Given a Hamiltonian action of a compact connected Lie group G on a symplectic manifold (M,ω) with moment map $\mu : M \to \mathfrak{g}^*$ and an orbit $\mathcal{O}$ of the coadjoint action of G on $\mathfrak{g}^*$. If the orbit consists of regular values of μ and the action of G on $\mu^{-1}(\mathcal{O})$ is free and proper, then the symplectic reduction $\mu^{-1}(\mathcal{O})/G$ is a symplectic manifold of dimension $dim(X) + dim(\mathcal{O}) - 2\,dim(G)$.*

[Hos]
The above theorem is an extension of the previous version by virtue of 0 always being a co-adjoint orbit as the co-adjoint action is linear. This extension will become useful in our later calculations of black holes, to solve isotopies that arise in the action on the momentmap. However removing these isotopies by choosing another orbit may not always be possible. In this case versions of this theorem exist that drop the requirement of the action being free entirely. In this case one doesn't end up with a simplectic space but rather a stratified symplectic space, with different regions for the different possible isotropies. A more extensive explanation can be found in [R S91].

3   Riemannian Geometry

Much like symplectic geometry, Riemannian geometry is it's own entire branch of differential geometry based on a structure induced by a 2-tensor. This 2-tensor is called the Riemannian metric, this metric locally defines distance on the manifold, and it connects naturally to the definition of connections and parallel transport. In our later physical applications we use pseudo-Riemannian metrics, which drop some of the conditions of Riemannian metrics, but maintain many of their useful properties.

3.1   The metric

Given a manifold M, a Riemannian metric g is a 2-tensor that defines an inner product on T_pM for each point p. We remember that an inner product $g\langle \cdot, \cdot \rangle$ on a vectorspace is defined as a symmetric bilinear function that is positive definite. This means for our 2-form g that it is symmetric and positive definite at each point $x \in M$. From the fact that it is positive definite, we can deduce that the form is also non-degenerate, and thus like with ω we have flat map

$$g^\flat : TM \to T^*M \tag{44}$$

$$g^\flat(X) = g\langle X, \cdot \rangle \tag{45}$$

and its inverse $g^\sharp$. These two maps are especially important in index notation, as they are what we use to lower and raise indices of vectors and covectors. We call (again for a chart χ):

$$X_\mu = X^\nu g_{\mu\nu} = \chi^* g^\flat(X) \tag{46}$$

$$\alpha^\mu = \alpha_\nu g^{\mu\nu} = \chi^* g^\sharp(\alpha) \tag{47}$$

Riemannian metrics are a great tool, they can also allow one to define distance on manifolds, which a priori is not a property manifolds possess, and they give a strong link between the tangent and cotangent spaces by serving as an inner product. For our purposes however, the Riemannian metric is a slightly too narrow definition. To be able to study general relativity we need to use Pseudo-Riemannian metrics.

Definition 3.1.1. A pseudo-Riemmanian metric on a manifold M is given by a 2-form g which is symmetric and non-degenerate. Symmetry means that for $x \in M$ and $v, w \in T_xM$ we have that $g_x(v, w) = g_x(w, v)$. Non-degenerateness means that for $x \in M$ there is no $v \in T_xM$ such that $\iota_v(g) = 0 \in T_x^*M$.

For specifically general relativity we take a Lorentzian metric, which has 4 dimensions, one negative eigenvalue and 3 positive eigenvalues. To see that this is a well defined idea we note that in coordinates, g can be written as a symmetric matrix at each point. In this case the 2-form is defined by

$$g_x(v, w) = \langle v, \mathrm{mat}_g w \rangle \tag{48}$$

Now we must remember a fact from linear algebra which states that Hermitian matrices have real eigenvalues.

Proposition 3.1.2. *A hermitian matrix has real eigenvalues.*

Proof. We take $\langle \cdot, \cdot \rangle$ the standard inner product on $\mathbb{C}^n$. Suppose $v \neq 0$, $Av = \lambda v$ and $A = A^\dagger$. Then:

$$\lambda = \frac{\langle v, Av \rangle}{\langle v, v \rangle} \tag{49}$$

$$= \frac{\langle Av, v \rangle}{\langle v, v \rangle} \tag{50}$$

$$= \frac{\lambda^* \langle v, v \rangle}{\langle v, v \rangle} \tag{51}$$

$$= \lambda^* \tag{52}$$

Since a real-symmetric matrix is hermitian, this will apply to such matrices. $\qquad\square$

We also remember that Hermitian matrices are diagonalizable.

Proposition 3.1.3. *A hermitian matrix is diagonalisable.*

Proof. We take $A = A^\dagger$ an $n \times n$ matrix with $Ax = \lambda x$. We take $x^\perp$ by the standard inner product on $\mathbb{C}^n$. We assume $|x| = 1$ and $y_2, .., y_n$ is an orthonormal basis of $x^\perp$. Then

$$0 = \langle y_i, x \rangle \tag{53}$$
$$= \langle y_i, Ax \rangle / \lambda \tag{54}$$
$$= \langle Ay_i, x \rangle / \lambda \tag{55}$$

So $Ay_i \in x^\perp$. This process can be repeated to find all n eigenvectors of A. $\qquad\square$

Since we require that the metric is non-degenerate everywhere, we can deduce that the sign of each of the eigenvalues cannot change. This is because we can, at least locally, apply the implicit function theorem to each zero of the characteristic polynomial as we move coordinates. Because of this we can say the definition of a Lorentzian metric is well posed.
The most common example of a Lorentzian metric is the Minkovski metric, which is given on $\mathbb{R}^4$ as

$$\eta_{\mu\nu} = diag(-1, 1, 1, 1) \tag{56}$$

That is, the diagonal matrix with one negative direction. In general relativity this is considered the ground state of the system, the lowest energy solution to Einsteins equations which we will discuss in another chapter.

3.2   Connections

Of course with this new structure come many compatible structures which we can use. One of the most important of these is the Levi-Civita connection. A connection gives a more general definition of a derivative on a vectorbundle. In general relativity we are especially interested in affine connections, which are connections on the tangent bundle of the manifold. The connection that we use in this case is the Levi-Civita connection ∇ which is defined uniquely by the metric with the following two properties

$$\nabla g = 0 \tag{57}$$
$$\text{and for any vector fields } X \text{ and } Y: \tag{58}$$
$$[X, Y] = \nabla_X Y - \nabla_Y X \tag{59}$$

The first property is called compatibility with the metric, the second property is called being torsion free. We now want to translate this structure into index notation. The existence and uniqueness of this connection was proven by T. Levi-Civita [Lev16], and is an often taught proof in many courses on vector bundles.
As mentioned before, in physics a manifold is often defined by a chart, rather than the entire smooth structure. When we choose these coordinates, the vectorfields that generate these coordinates are commuting, so for instance in polar coordinates

$$[X_r, X_\phi] = \partial_r \partial_\phi - \partial_\phi \partial_r = 0 \tag{60}$$

In physics we also say the coordinates are non-degenerate. As we generally only work in coordinates in physics there tends to be a slight disconnect between derivatives and vectorfields that is not there in pure manifold theory, we often distinguish between X^μ a vectorfield and $X^\mu \partial_\mu = \mathcal{L}_X$ the derivative it generates. Now to numerically evaluate the connection we use Christoffel symbols, which are analogous to the connection form one can use to describe the connection. For a vector or one-form we write:

$$\nabla_\mu x^\nu = \partial_\mu x^\nu + \Gamma^\nu_{\mu\rho} x^\rho \tag{61}$$

We note that by the product rule for ∇:

$$\partial_\mu(x^\nu \alpha_\nu) = \nabla_\mu(x^\nu \alpha_\nu) := \tag{62}$$
$$= \nabla(x^\nu)\alpha_\nu + x^\nu \nabla(\alpha_\nu) \tag{63}$$
$$= \partial_\mu(x^\nu)\alpha_\nu + \Gamma^\nu_{\mu\rho} x^\rho \alpha_\nu + x^\nu \nabla(\alpha_\nu) \tag{64}$$
$$\tag{65}$$

and by the product rule for ∂ we can say this is equal to:

$$\partial_\mu(x^\nu)\alpha_\nu + x^\nu\partial_\mu(\alpha_\nu) \tag{66}$$

so we can conclude

$$\nabla_\mu\alpha_\nu = \partial_\mu\alpha^\nu - \Gamma^\rho_{\mu\nu}\alpha_\rho \tag{67}$$

In the same way we can for 2-forms (and higher order tensor forms):

$$\nabla_\rho g_{\mu\nu} = \partial_\rho g_{\mu\nu} - \Gamma^\sigma_{\mu\rho}g_{\sigma\nu} - \Gamma^\sigma_{\nu\rho}g_{\mu\sigma} \tag{68}$$

We now have enough information to describe $\Gamma^\rho_{\mu\nu}$. We first note that the no torsion condition

$$[X,Y] = \nabla_X Y - \nabla_Y X \tag{69}$$

Translates in index notation to

$$X^\mu\nabla_\mu Y^\nu - Y^\mu\nabla_\mu X^\nu = X^\mu\partial_\mu Y^\nu - Y^\mu\partial_\mu X^\nu \tag{70}$$

which means that the Christoffel symbol is symmetric in the lower two indices: $\Gamma^\rho_{\mu\nu} = \Gamma^\rho_{\nu\mu}$. We can now calculate the values of these Christoffel symbols using the compatibility with the metric:

$$0 = \nabla_\rho g_{\mu\nu} \tag{71}$$
$$\partial_\rho g_{\mu\nu} = \Gamma^\sigma_{\mu\rho}g_{\sigma\nu} + \Gamma^\sigma_{\nu\rho}g_{\mu\sigma} \tag{72}$$
$$\partial_\rho g_{\mu\nu} = \Gamma^\sigma_{\mu\rho}g_{\sigma\nu} + \Gamma^\sigma_{\nu\rho}g_{\mu\sigma} \tag{73}$$
$$2\Gamma^\sigma_{\mu\nu}g_{\sigma\rho} = \partial_\mu g_{\nu\rho} + \partial_\mu g_{\mu\rho} - \partial_{rho}g_{\mu\nu} \tag{74}$$
$$\Gamma^\sigma_{\mu\nu} = \tfrac{1}{2}g^{\sigma\rho}\left(\partial_\mu g_{\nu\rho} + \partial_\mu g_{\mu\rho} - \partial_\rho g_{\mu\nu}\right) \tag{75}$$

For a more in-depth explanation of this calculation one can check [Car19]. The last line is also known as Koszuls theorem.

3.3   Curvature

An important property of a metric on a manifold is it's curvature at a point. An often used tool for this is the so called Riemann Curvature tensor, defined by

$$R(X,Y)(Z) = \nabla_X\nabla_Y Z - \nabla_Y\nabla_X Z - \nabla_{[X,Y]}Z \tag{76}$$

Where ∇ is the Levi-Civita connection associated with the metric g. We want to translate this to coordinates and the index notation, as this often makes calculations much easier, and most physics equations are defined in those coordinates. For these coordinates we remember that we can say $[X_\mu, X_\nu] = 0$, and so

$$R^\mu_{\nu\rho\sigma}Z^\sigma = \nabla_\nu\nabla_\rho Z^\mu - \nabla_\rho\nabla_\nu Z^\mu \tag{77}$$
$$R^\mu_{\nu\rho\sigma} = \partial_\rho\Gamma^\mu_{\nu\sigma} - \partial_\sigma\Gamma^\mu_{\nu\rho} + \Gamma^\mu_{\rho\lambda}\Gamma^\lambda_{\sigma\nu} - \Gamma^\mu_{\sigma\lambda}\Gamma^\lambda_{\rho\nu} \tag{78}$$

For the full calculation one can read [Car19]. Note that this calculation does use that there is no torsion.

3.4   Lagrangians and Hamiltonians in Physics

One of the more important parts of Riemannian and Pseudo-Riemannian geometry is the study of geodesics. On a Riemannian manifold such geodesics are described as the locally shortest paths. On a curved space these geodesics take the place of straight lines.

In physics, dynamics can be described in multiple ways, the simplest being the Newtonian formulation. In this formulation, the dynamics of a system are described by forces, and the movement of a particle is described

by $\ddot{q} = F/m$ where q is the position of the particle, m the mass and F the force acting on the particle. However this method has it's limits, and cannot for instance describe the motion of a particle on a general (pseudo)-Riemannian manifold. To find the equations of motion on such a manifold the principle of least action can be used. We will not go into the entire principle here, but we will give a short description. For a particle moving a long a path given by $q : \mathbb{R} \to M$, the action is given by:

$$S = \int \mathcal{L}(q(\tau), \dot{q}(\tau)) d\tau \tag{79}$$

Where $\mathcal{L}$ is the Lagrangian, this is in general a function on TM. To calculate whether a path gives a local minimum of the action we would have to walk through some calculus of variation, however this will not be extremely useful for understanding the further math, so we leave it to the following book: SOURCE.

It is useful for us to know the conclusion, which is that the action is locally minimal for q if

$$\frac{\partial \mathcal{L}}{\partial q} - \frac{d}{d\tau} \frac{\partial \mathcal{L}}{\partial \dot{q}} = 0 \tag{80}$$

This is called the Euler Lagrange equation, and it describes a vectorfield in TM.

The Lagrangian description of a system is related to the Hamiltonian one by the Legendre transform. We will first define this transform on a vectorspace, after which we will extend it to the tangent space TQ of a manifold Q.

Definition 3.4.1. Given a vectorspace V and a function $L : V \to \mathbb{R}$ we define a derivative $DL : V \to V^*$ via the expected way

$$DL(v)(w) = \frac{d}{d\tau}\bigg|_{\tau=0} L(v + \tau w) \tag{81}$$

We now ask that this DL is injective, this is equivalent with asking that the Hessian of L is non-degenerate. It is then invertible (as V^* and V share dimension, both being finite). We define:

$$L^* = L \circ DL^{-1} : V^* \to \mathbb{R} \tag{82}$$

As the Legendre transform of L.

Next we want to translate this from vectorspaces to tangent spaces. We take a manifold Q, with a Lagrangian $\mathcal{L} : TQ \to \mathbb{R}$. Next we define a map $d\mathcal{L}_q : T_qQ \to T_q^*Q$ in much the same way as above, however here do it pointwise:

$$D\mathcal{L}_q(v)(w) = \frac{d}{d\tau}\bigg|_{t=0} \mathcal{L}(q, v + \tau w) \tag{83}$$

We then take the pointwise inverse of $D\mathcal{L}$ and define $\mathcal{L}^* = \mathcal{L} \circ D\mathcal{L}^{-1}$. Next we want to show that the Hamiltonian dynamics of this Legendre transform indeed coincide with those of the Lagrangian. To see this we will show that the dynamics of Euler-Lagrange equations coincide with those of the Hamiltonian vector field, when restricted to Q. We will however only do this for the specific case of pseudo-Riemannian geodesics.

3.5 The Legendre Transform for Pseudo-Riemannian geodesics

We take (Q, g) a Riemannian manifold, and (T^*Q, ω) a symplectic manifold with ω the canonical symplectic form. The Lagrangian description of a free particle gives us a map

$$\mathcal{L} : TQ \to \mathbb{R} \tag{84}$$
$$(q, v) \mapsto \tfrac{1}{2} g_q(v, v) \tag{85}$$

We will now show that we can use a Legendre transform and turn this Lagrangian into a Hamiltonian system. First we define our Legendre transform. We start by calculating $D\mathcal{L}$. We see that

$$D\mathcal{L}_q(v)(w) = g_q(v, \cdot)(w) \tag{86}$$
$$= p(w) \tag{87}$$

We call p the momentum. We now see, using invertibility of g

$$H(q,p) = \mathcal{L}L \circ D\mathcal{L}_q^{-1}(p) \tag{88}$$

$$= \mathcal{L}(q, g^\sharp(p)) \tag{89}$$

$$= \tfrac{1}{2} g_q(g^\sharp(p), g^\sharp(p)) \tag{90}$$

We will now show that the Hamiltonian defined above actually encodes the dynamics of the geodesics on a pseudo-Riemannian manifold. We note that the dynamics of vectorfields is a local property, and we can thus work in charts. It only remains for us to show that the Hamiltonian and Lagrangian describe the same dynamics on $\mathbb{R}^4$ with an arbitrary Pseudo-Riemannian metric g.

To start, we see that the Liouville form on $T^*\mathbb{R}^4 = (\mathbb{R}^4)^* \oplus \mathbb{R}^4$ is given by

$$\lambda : \left((\mathbb{R}^4)^* \oplus \mathbb{R}^4 \right) \oplus \left((\mathbb{R}^4)^* \oplus \mathbb{R}^4 \right) \to \mathbb{R} \tag{91}$$

$$(\alpha, v, p, q) \mapsto p(v) \tag{92}$$

Here $(\mathbb{R}^4)^*$ is the fibre term. This means we can define the symplectic form $\omega = -d\lambda$ as:

$$\omega : \left((\mathbb{R}^4)^* \oplus \mathbb{R}^4 \right) \oplus \left((\mathbb{R}^4)^* \oplus \mathbb{R}^4 \right) \oplus \left((\mathbb{R}^4)^* \oplus \mathbb{R}^4 \right) \to \mathbb{R} \tag{93}$$

$$(\alpha, v, \beta, w, p, q) \mapsto \alpha(w) - \beta(v) \tag{94}$$

We now look again at the Lagrangian of the geodesic motion on $T\mathbb{R}^4$, we also translate to index notation as we are working in coordinates on $\mathbb{R}^4$:

$$\mathcal{L}(q,v) = \tfrac{1}{2} g(v,v) = \tfrac{1}{2} g_{\mu\nu} v^\mu v^\nu \tag{95}$$

Using the Euler-Lagrange equations we get the geodesic equation, for the full calculation see [Car19]:

$$\frac{d^2}{d\tau^2} q^\mu + \Gamma^\mu_{\rho\sigma} \frac{d}{d\tau} q^\rho \frac{d}{d\tau} q^\sigma = 0 \tag{96}$$

Where

$$\Gamma^\mu_{\rho\sigma} = \tfrac{1}{2} g^{\mu\nu} (\partial_\rho g_{\mu\sigma} + \partial_\sigma g_{\mu\rho} - \partial_\mu g_{\rho\sigma}) \tag{97}$$

We compare this to the dynamics of the Hamiltonian on $T^*\mathbb{R}^4$, given by

$$H(p,q) = \frac{g(g^\sharp(p), g^\sharp(p))}{2} = \frac{g^*(p,p)}{2} \tag{98}$$

We calculate the Hamiltonian vectorfield X_H. We remember the definition

$$\omega_{p,q}(X_H, \cdot) = dH_{p,q} \tag{99}$$

Now let $(\alpha, v) \in T(T^*_{p,q}\mathbb{R}^4)$. We calculate

$$dH_{p,q}(\alpha, v) = \mathcal{L}_{(\alpha,v)} H|_{(p,q)} \tag{100}$$

$$= \mathcal{L}_{(\alpha,0)} H|_{(p,q)} + \mathcal{L}_{(0,v)} H|_{(p,q)} \tag{101}$$

$$= \frac{d}{d\tau}\bigg|_{\tau=0} H(p + \tau\alpha, q) + \frac{d}{d\tau}\bigg|_{\tau=0} H(p, q + \tau v) \tag{102}$$

$$= \frac{d}{d\tau}\bigg|_{\tau=0} \frac{g^*_q(p + \tau\alpha, p + \tau\alpha)}{2} + \frac{d}{d\tau}\bigg|_{\tau=0} \frac{g^*_{q+\tau v}(p, p)}{2} \tag{103}$$

$$= g^*(p, \alpha) + \frac{(\mathcal{L}_v g^*)(p,p)}{2} \tag{104}$$

So we can say that

$$dH_{p,q} = g^*(p, \pi_p) + \frac{(\mathcal{L}_q g^*)(p,p)}{2} \pi_q \tag{105}$$

where π_p is the projection to the fibre and it's tangent space, so to $T(\mathbb{R}^4)^* \subset T(T^*\mathbb{R}^4)$, meanwhile π_q is the projection to the manifold part of the chart, so to $T\mathbb{R}^4 \subset T(T^*\mathbb{R}^4)$.

$$X_{H,(p,q)} = \omega_{p,q}^{\sharp}\left(g^*(p,\pi_p) + \frac{(\mathcal{L}_{\pi_q}g^*)(p,p)}{2}\right) \tag{106}$$

Here we use τ as the variable of the parametrisation:

$$\partial_\tau(q,p) = X_{H,(q,p)} \tag{107}$$

and so

$$\frac{d}{d\tau}q = g^{\sharp}(p) \tag{108}$$

$$\frac{d}{d\tau}p = -\frac{(\mathcal{L}_q g^*)(p,p)}{2} \tag{109}$$

We now want to translate this to index notation, to get the geodesic equation 96.
Rewriting the above into index notation we are given:

$$\frac{d}{d\tau}q^\mu = g^{\mu\nu}p_\nu \tag{110}$$

$$\frac{d}{d\tau}p_\mu = -\frac{(\partial_\mu g^{\rho\sigma})p_\sigma p_\rho}{2} \tag{111}$$

We will now show that these align with the usual definition for the geodesic equation:

$$\frac{d^2}{d\tau^2}q^\mu = \frac{d}{d\tau}(g^{\sharp}p)^\mu \tag{112}$$

$$= \frac{d}{d\tau}(g^{\mu\sigma}p_\sigma) \tag{113}$$

$$= \frac{d}{d\tau}(g^{\mu\sigma})p_\sigma + g^{\mu\sigma}\frac{d}{dt}p_\sigma \tag{114}$$

$$= \left(\frac{d}{d\tau}q^\rho\right)(\partial_\rho g^{\mu\sigma})p_\sigma - g^{\mu\sigma}\partial_\sigma H \tag{115}$$

$$= (\tfrac{d}{d\tau}q^\rho)(\partial_\rho g^{\mu\sigma})g_{\nu\sigma}\tfrac{d}{d\tau}q^\nu - \tfrac{1}{2}g^{\mu\sigma}\partial_\sigma g^{\rho\nu}p_\rho p_\nu \tag{116}$$

$$= \tfrac{1}{2}g^{\mu\nu}\left(-\partial_\nu g_{\rho\sigma} + \partial_\sigma g_{\rho\nu} + \partial_\rho g_{\sigma\nu}\right)\tfrac{d}{d\tau}q^\sigma\tfrac{d}{d\tau}g^\rho \tag{117}$$

In the last line the the first term was made symmetric in $\rho\sigma$, as the $p_\rho p_\sigma$ is also symmetric, and indeces were lifted/lowered to conform with the usual definition of Γ without torsion.
We have now shown that the Hamiltonian and Lagrangian description give the same dynamics in coordinates, and since this is a local property we can state the same for general pseudo-Riemannian manifolds.

4 Quick introduction to GR

General relativity is a theory that expands on Einsteins Special relativity by allowing not only for fixed velocity reference frames, but also accelerating ones. It expands on the two postulates of a universal speed of light and no central reference frame with a third, the equivalence principle. This states that gravity cannot be distinguished from being in an accelerating reference frame.

The math of general relativity is built on that of pseudo-Riemannian geometry. Specifically its structure is a 4-dimensional manifold with a pseudo-Riemannian metric with 1 negative and 3 positive eigenvalues. This is often called a Lorentzian manifold. This metric is given by $g_{\mu\nu}$, which is governed by the Einstein-Hilbert action, a more elaborate treatment of this action can be found in [Car19].

$$S = \frac{c^4}{8\pi G} \int R\sqrt{-g}d^4x \tag{118}$$

Here R is the Ricci scalar, defined by the Ricci tensor $Ric_{\mu\nu}$:

$$R = Ric_{\mu\nu}g^{\mu\nu} \tag{119}$$

The Ricci tensor is given by a trace of the Riemann tensor

$$Ric_{\mu\nu} = R^{\rho}_{\mu\rho\nu} \tag{120}$$

The equation of motion of this action is given by

$$Ric_{\mu\nu} - \tfrac{1}{2}Rg_{\mu\nu} = 0 \tag{121}$$

or, if we add mass couplings to the action, by

$$Ric_{\mu\nu} - \tfrac{1}{2}Rg_{\mu\nu} = \frac{8\pi G}{c^4}T_{\mu\nu} \tag{122}$$

With $T_{\mu\nu}$ the energy-momentum tensor of the matter coupling terms in the action. We will mostly be interested in the first version of this equation, which governs the behaviour of the metric in vacuum. A lot of interesting vaccuum solutions exist, such as the solution that gives gravitational waves propagating through vaccuum. The solutions we will be looking at are known as stationary axi-symmetric vaccuum solutions, stationary meaning that the solution does not change with the time coordinate, and axi-symmetric meaning that the solution has a rotational symmetric around some axis.

For some given metric, the Hamiltonian of geodesic movement is given as we defined it before by

$$H(p,q) = \frac{g^{\mu\nu}p_{\mu}p_{\nu}}{2} \tag{123}$$

There are 3 distinct sets of geodesics now. The first is given by the levelsets $H < 0$ are called timelike, physically speaking this defines the possible paths of an object with mass. The geodesics in the levelset with $H = 0$ give the lightlike paths, as the name suggests these are the geodesics photons and other massless objects follow. The last set given by the levelsets $H > 0$, these are called spacelike geodesics and considered non-physical paths for any object to follow.

5   Black holes

In this chapter we will discuss different SAV-solutions of the Einstein equation. The most interesting of these solutions are black holes, often given by a singularity enclosed by an event horizon, past which no space- or lightlike geodesics can travel outward.

5.1   The Schwarzschild Spacetime

A much studied spacetime in general relativity is the black hole solution first posed by Schwarzschild [Sch16]. This metric is given in polar coordinates, in units with $c = 1$ below:

$$g_{\mu\nu} = -\left(1 - \frac{2GM}{r}\right)dt^2 + \left(1 - \frac{2GM}{r}\right)^{-1} dr^2 + r^2 d\theta^2 + r^2 \sin^2\theta d\phi^2 \tag{124}$$

on the manifold $\mathbb{R}_t \times \{r > 0 | r \neq 2GM\}_r \times (0, \pi)_\theta \times \mathbb{R}_\phi$. Here M is the mass of the black hole. The derivation that this is indeed a vaccuum solution of GR can be found in [Car19]. The thing that makes this spacetime special is that it was the first discovered case of a static vacuum solution that was not flat, that is to say, it has a non-zero Riemannian curvature tensor. In fact this is a vaccuum solution that exhibits a curvature singularity at $r = 0$. As one gets closer to the singularity, time is curved inward more and more. Once the radius goes below $r = 2GM$, often called the Schwarzschild radius, the t and r components of the metric flip their sign, and physical time flows not forward in the t direction but downward in the r direction. Any geodesics passing this border cannot return, this is called the event horizon.

Figure 1: The shadow of a Schwarzschild black hole. Steller background by: ESO/S. Brunier [Bru]

5.1.1 Symplectic reduction and dynamics

We are interested in the geodesic structure of this pseudo-Riemannian manifold. For this we will use the tools of symplectic and Hamiltonian geometry. It is clear from the structure of the metric that this is a spherically symmetric spacetime. Mathematically this means that our space obeys a symmetry under the Lie group $SO(3)$. In this case the vectorfields that generate the action by $SO(3)$ are given by:

$$X_1 = \partial_\phi \tag{125}$$
$$X_2 = \sin(\phi)\partial_\theta - \cos(\phi)\partial_\phi \tag{126}$$
$$X_3 = \cos(\phi)\partial_\theta - \sin(\phi)\partial_\phi \tag{127}$$

It is clear that X_1, X_2, X_3 obey the algebra of $SO(3)$ given by

$$[X_1, X_2] = \partial_\phi(\sin(\phi)\partial_\theta - \cos(\phi)\partial_\phi) - (\sin(\phi)\partial_\theta - \cos(\phi)\partial_\phi)\partial_\phi = \cos(\phi)\partial_\theta - \sin(\phi)\partial_\phi = X_3 \tag{128}$$
$$[X_2, X_3] = (\sin(\phi)\partial_\theta - \cos(\phi)\partial_\phi)(\cos(\phi)\partial_\theta - \sin(\phi)\partial_\phi) - (\cos(\phi)\partial_\theta - \sin(\phi)\partial_\phi)(\sin(\phi)\partial_\theta - \cos(\phi)\partial_\phi) \tag{129}$$
$$= (\cos^2\phi + \sin^2\phi)\partial_\phi + (\sin\phi\cos\phi - \cos\phi\sin\phi)\partial_\theta = \partial_\phi = X_1 \tag{130}$$
$$[X_3, X_1] = (\cos(\phi)\partial_\theta - \sin(\phi)\partial_\phi)\partial_\phi - \partial_\phi\cos(\phi)\partial_\theta - \sin(\phi)\partial_\phi = \sin(\phi)\partial_\theta - \cos(\phi)\partial_\phi = X_2 \tag{131}$$

As such our symmetry group is given by $SO(3)$. We next try to write down a momentum map for this symmetry. We see that using lemma 2.5.3:

$$\mu(p, q)(\xi) = \lambda_{p,q}(\xi) \tag{132}$$
$$= \sum_i p_i dq_i(X_\xi) \tag{133}$$
$$\tag{134}$$

As such we can write

$$\mu : \mathbb{T}^*\mathbb{R}^4 \to \mathfrak{so}^*(3) \tag{135}$$
$$(q, p) \mapsto (L_1(p, q), L_2(p, q), L_3(p, q)) \tag{136}$$

where L_i are given by what in physics is called the angular momentum

$$L_1 = p_\phi \tag{137}$$
$$L_2 = \sin(\phi)p_\theta + \cos(\phi)p_\phi \tag{138}$$
$$L_3 = \cos(\phi)p_\theta - \sin(\phi)p_\phi \tag{139}$$

Here p_ϕ is the dual coordinate of ∂_ϕ, p_θ is the dual coordinate of ∂_θ.

For the actual reduction we do need to check that G acts freely on $\mu^{-1}(0)$. Sadly we can immediately see that the rotations of a sphere are fixed along their axis. We can immediately conclude this action is not free and thus we cannot apply the standard Marsden-Weinstein theorem to the Hamiltonian group action we found. This leaves us with three options.

Firstly we can instead choose another co-adjoint orbit in $\mathfrak{so}^*(3)$. The orbits in this dual algebra are given by spheres. To be able to make clearer statements about the symmetries and pullbacks it will however be easier to work in cartesian coordinates. However we will not translate the metric to cartesian coordinates, we will merely remember it's Hamiltonian is spherically symmetrical. In this case we know the generators of the group are given by

$$X_1 = x\partial_y - y\partial_x \tag{140}$$
$$X_2 = y\partial_z - z\partial_y \tag{141}$$
$$X_3 = z\partial_x - x\partial_z \tag{142}$$

with momenta given by

$$L_1 = xp_y - yp_x \tag{143}$$
$$L_2 = yp_z - zp_y \tag{144}$$
$$L_3 = zp_x - xp_z \tag{145}$$

by similar calculations as above. We see that the pullback of a sphere in $\mathfrak{so}^*(3)$ is now given by $S^1(\mathbb{R}^3 \setminus \{0\}) \times T^*\mathbb{R}$. Here $(\mathbb{R} \times S^1)(\mathbb{R}^3 \setminus \{0\})$ is a cylinder bundle lying in $T^*\mathbb{R}^3$ exactly such that the circles lie perpendicular to the point. We see that where we had an isotopy of type S^1 at each point before, under the $SO(3)$ action, we have now fixed that isotopy by adding this extra circle at each point. Our action is now free and our reduction valid.

If however we do also want to do the full reduction at $\mu^{-1}(0)$, we will have to apply the result by [R S91]. This states that we can still reduce without the action being free, however we end up not with a symplectic space bnut a stratified symplectic space. This space has components for every possible isotopy we can find in our action. Since there is only one such isotopy, namely an S^1 isotopy for every point for exactly the group elements of which it is an axis of rotation, the space will still be a symplectic manifold.

Lastly what we could do is we could reduce the dimension of our symmetry group. We would use $SO(2)$ rather than $SO(3)$. This group only gives the rotations around the ϕ axis, which we would then have to remove from the space for the action to be free. This is what we would have to do in later cases of black holes, as these will no longer be spherically symmetric but only axi-symmetric.

Next we look at another symmetry of our system generated by the vectorfield

$$X = \partial_t \tag{146}$$

This has momentum map

$$\mu(p, q) = p_t \tag{147}$$

However, when reducing by this symmetry we can no longer choose p_t freely such that our entire reduced space lies in the levelset of $H = 0$. We would like to be able to do this to be able to look exclusively at lightlike geodesics.

So we now look back at our proposition 2.3.3 and remember that the dynamics of H are purely determined by it's levelsets, and as such the dynamics of lightlike geodesics are entirely determined by the 0 levelset of H. This means we can freely multiply it with a non-zero function without disturbing those dynamics, as seem in lemma 2.3.4. We multiply H by $1 - \frac{2GM}{r}$, this function is zero if $r = 2GM$, but since our Hamiltonian is not defined there, we can consider this function non-zero.

$$H' = \left(1 - \frac{2GM}{r}\right)H = \frac{1}{2}\left(-p_t^2 + \left(1 - \frac{2GM}{r}\right)^2 p_r^2 + \left(1 - \frac{2GM}{r}\right)r^{-2}(p_\theta^2 + \sin^{-2}\theta p_\phi^2)\right) \tag{148}$$

This system still holds the same symmetries as before and as such our Hamiltonian group action and momentum map are still valid. And thus we can still do our full reduction, either for zero or non-zero co-adjoint orbits of the momentum.

Moreover we gained an extra useful property which is that we can choose p_t to be any value without affecting the dynamics of other coordinates at all, as it is completely separated. This means that the dynamics at any p_t are the same as they would be at p_t such that $H' = H = 0$. If we now reduce by the t direction we are left with a two-dimensional space $\mathbb{R}_{\geq 0} * \mathbb{R}^*$ with the canonical symplectic form and the Hamiltonian given by

$$H' = \frac{1}{2}\left(\left(1 - \frac{2GM}{r}\right)^2 p_r^2 + \left(1 - \frac{2GM}{r}\right)r^{-2}p_\phi^2\right) \tag{149}$$

We can see the flow of this Hamiltonian in figure 2.

Sadly this version of the Hamiltonian has a more difficult equation for geodesics movement due to reparametrisation. While it provides a reduction to exactly the space of lightlike geodesics in only the r coordinates, it is more useful to preform the last reduction without the multiplication if we want to explore the dynamics of lightlike geodesics analytically.

5.1.2   Effective potential

In physics we often describe the motion of particles in a given spacetime using effective potentials. Especially for the Schwarzschild metric this makes the geodesic dynamics significantly easier to interpret, as we only
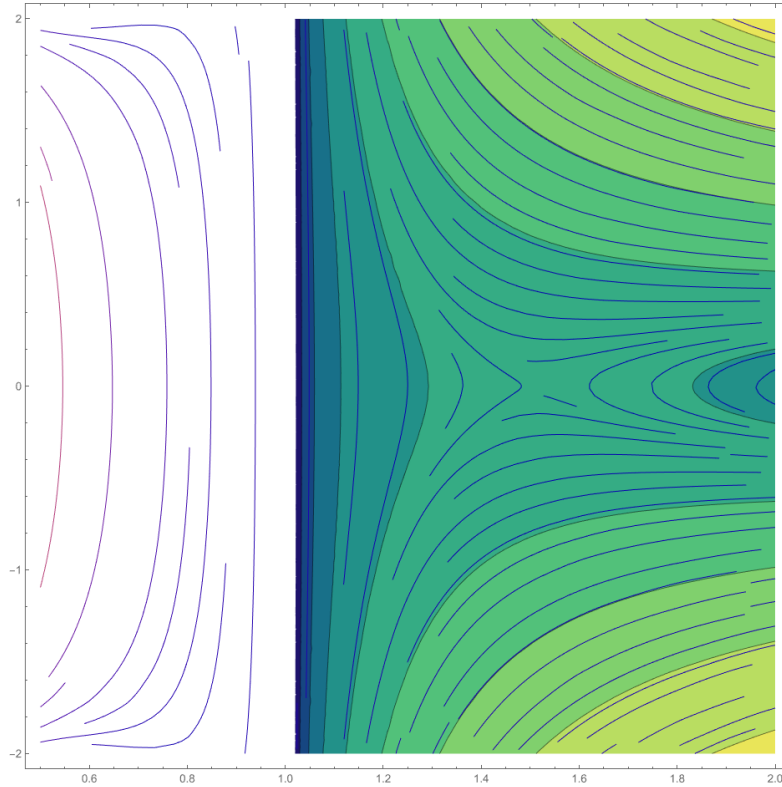
Figure 2: The flow and levelsets of the corrected Hamiltonian for light flow, the horizontal axis is for r, the vertical axis is for p_r. This plot is for $M = 0.5$ and $p_\phi = 1$. Note the only fixed point lying at 3GM from the centre. The levelsets of the Hamiltonian are also plotted outside the event horizon, clearly visible by the vertical line in the flow.

have one dimension in which the dynamics are not given by a conserved momentum. We want to write an effective Hamiltonian such that the dynamics of this Hamiltonian are the same as those of our original Hamiltonian after reduction. We write this in the coordinate r as:

$$H_{eff}(r, p_r) = \tfrac{1}{2}p_r^2 + V(r) \tag{150}$$

where V is called the effective potential. The dynamics of this Hamiltonian are given by

$$\dot{r} = p_r \tag{151}$$
$$\dot{p_r} = -\partial_r V(r) \tag{152}$$

Or alternatively

$$\ddot{r} = -\partial_r V(r) \tag{153}$$
$$\tag{154}$$

We want to find the potential V such that the dynamics of r follow these dynamics. We mostly follow the calculations as done in [Car19].

We remember that the metric was given by equation 124. We will try to write down the equations of motion for r, in terms of the constants H, p_ϕ. We will again use the variable τ to denote the parametrization. We remember the Hamiltonian equations for the dynamics given in equation 108, we evaluate these:

$$\partial_\tau p_r = -\tfrac{1}{2}\partial_r g^{\mu\nu}p_\mu p_\nu \tag{155}$$

$$= \frac{2GM}{r^2}p_r^2 + \frac{2GM}{r^2}\left(1 - \frac{2GM}{r}\right)^{-2}p_t^2 - \frac{2}{r^3}p_\phi^2 \tag{156}$$

and

$$\partial_\tau r = \left(1 - \frac{2GM}{r}\right) p_r \tag{157}$$

Combining the two we can see

$$\partial_\tau^2 r = \partial_\tau \left(1 - \frac{2GM}{r}\right) p_r \tag{158}$$

$$= \left(1 - \frac{2GM}{r}\right) \partial_\tau p_r + p_r \frac{2GM}{r^2} \partial_\tau r \tag{159}$$

$$= \left(1 - \frac{2GM}{r}\right) \partial_\tau p_r + \frac{2GM}{r^2} \left(1 - \frac{2GM}{r}\right) p_r^2 \tag{160}$$

$$= -\frac{1}{2}\left(1 - \frac{2GM}{r}\right)\left(\frac{2GM}{r^2}p_r^2 + \frac{2GM}{r^2}\left(1 - \frac{2GM}{r}\right)^{-2}p_t^2 - \frac{2}{r^3}p_\phi^2\right) + \frac{2GM}{r^2}\left(1 - \frac{2GM}{r}\right)p_r^2 \tag{161}$$

$$= \frac{1}{2}\frac{2GM}{r^2}\left(\left(1 - \frac{2GM}{r}\right)p_r^2 - \left(1 - \frac{2GM}{r}\right)^{-1}p_t^2 + \frac{2}{r^3}\frac{r^2}{2GM}\left(1 - \frac{2GM}{r}\right)p_\phi^2\right) \tag{162}$$

$$= \frac{GM}{r^2}\left(-\left(1 - \frac{2GM}{r}\right)^{-1}p_t^2 + \left(1 - \frac{2GM}{r}\right)p_r^2 + r^{-2}p_\phi^2\right) \tag{163}$$

$$+ \frac{p_\phi^2}{r^3} - \frac{3GMp_\phi^2}{r^4} \tag{164}$$

$$= \frac{2GM}{r^2}H + \frac{p_\phi^2}{r^3} - \frac{3GMp_\phi^2}{r^4} \tag{165}$$

So if we want to see this as a central potential, we write this as

$$\ddot{r} = -\frac{dV}{dr} \tag{166}$$

$$= \frac{GM}{r^2}H + \frac{p_\phi^2}{r^3} - \frac{3GMp_\phi^2}{r^4} \tag{167}$$

$$= -\frac{d}{dr}\left(-\frac{GM}{r}H + \frac{p_\phi^2}{2r^2} - \frac{GMp_\phi^2}{r^3}\right) \tag{168}$$

So our effective potential becomes

$$V(r) = -\frac{GM}{r}H + \frac{p_\phi^2}{2r^2} - \frac{GMp_\phi^2}{r^3} \tag{169}$$

Since we are mostly interested in null-geodesics we set $p^2 \to 0$ and so

$$V(r) = \frac{p_\phi^2}{2r^2} - \frac{GMp_\phi^2}{r^3} \tag{170}$$

We see this potential plotted in figure 3.

5.1.3   Periodic Photon Orbits

We can see from the above figure, and also from the description of the effective potential, that it has a peak at $r = 3GM$. Since the dynamics of the effective Hamiltonian are given by equation 153, we see that periodic lightlike geodesics are given only by those that lie at $r = 3GM$ with no radial momentum. This encodes exactly all lightlike periodic orbits of the Schwarzschild black hole.
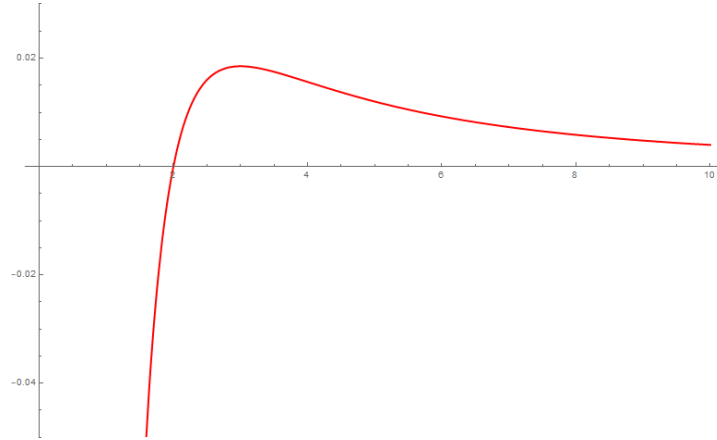
Figure 3: The effective potential for $p_\phi^2 = 1$ and $GM = 1$.

5.2   The Kerr Spacetime

5.2.1   The Kerr Metric

Where the Schwarzschild solution gives the spacetime of a non-rotating black hole, the Kerr spacetime gives a more general solution of a black hole that is rotating, rather than entirely spherically symmetric like the Schwarzschild case. The metric is given by

$$g_{\mu\nu} = -\left(1 - \frac{2GMr}{\rho}\right)dt^2 + \frac{\rho^2}{\delta}dr^2 + \rho^2 d\theta^2 + \frac{2GMar\sin^2\theta}{\rho^2}(d\phi dt + dt d\phi) + \frac{\sin^2\theta}{\rho^2}\left((r^2 + a^2)^2 - a^2\Delta\sin^2\theta\right)d\phi^2$$

(171)

with

$$\Delta(r) = r^2 - 2GMr + a^2 \tag{172}$$

$$\rho^2 = r^a + a^2\cos^2\theta \tag{173}$$

$$a = S/M \tag{174}$$

, where S is the spin of the black hole. The coordinates of the metric are called Boyer-Lindquist coordinates, these are given by

$$t = t \tag{175}$$

$$x = \sqrt{r^2 + a^2}\sin\theta\cos\phi \tag{176}$$

$$y = \sqrt{r^2 + a^2}\sin\theta\sin\phi \tag{177}$$

$$z = r\cos\theta \tag{178}$$

$$\tag{179}$$

. For a more detailed explanation on this one can follow [Car19], or the original article by Kerr [Ker63], however the latter uses different coordinates.

5.2.2   Periodic Photon Orbits

In the Kerr spacetime too there are periodic photon orbits. However these can be much more complicated because one of the dimensions of symmetry is lost. For an exact symbolic analysis of the foton orbits of the Kerr black hole one can look at [CF 16]. We will later do numerical simulations of such geodesics, and we will see a few qualitative changes compared to the Schwarzschild non-rotating case. The most important qualitative difference is that null-orbits travelling prograde to the rotation lie at a much smaller radius than those travelling retrograde. Prograde in this case means they are travelling in the same direction as the spin. This can be compared to how in a whirlpool its much easier to travel along the flow than against it.
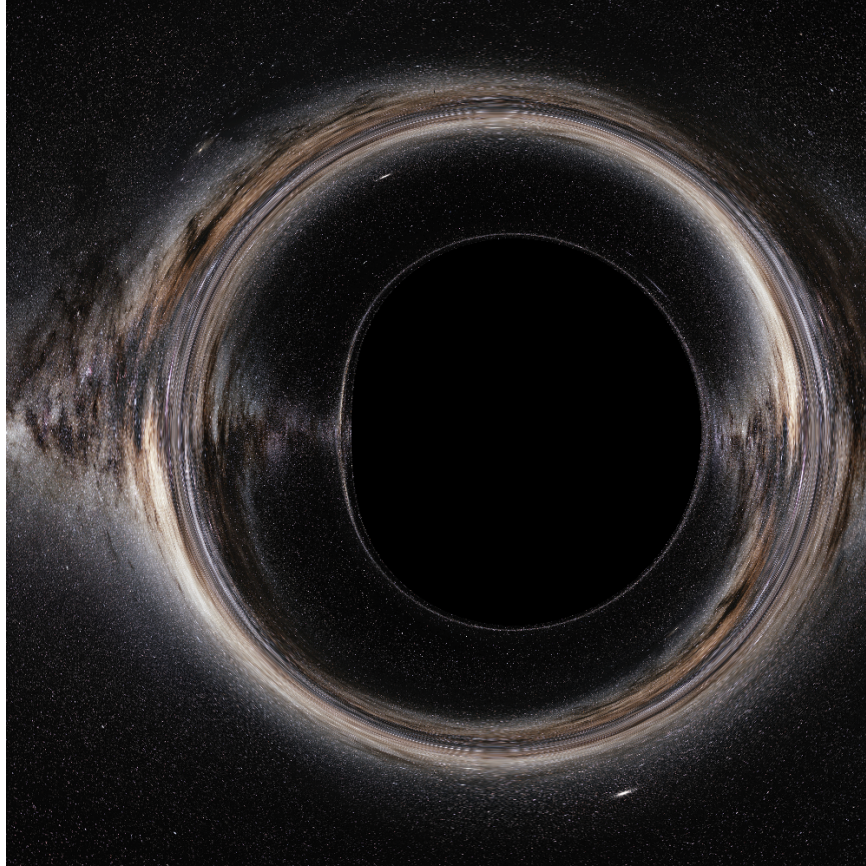
Figure 4: The shadow of a Kerr black hole. Steller background by: ESO/S. Brunier [Bru]

5.3   Manko Novikov Spacetime

As Kerr expanded the Schwarzschild spacetime by adding a dipole current-moment, Manko and Novikov expanded this spacetime further by adding additional higher order multipole mass moments [MN92]. Like the Kerr solution this is still a stationary and axi-symmetric vaccuum solution of Einsteins equation. However it has some issues that could dequalify it from being a physical solution, such as that it has a curvature singularity on the horizon, meaning it does not follow the censorship conjecture. It also loses integrability of the geodesic dynamics, because unlike Kerr it does not have an extra constant of motion called the Carter constant [Bri08]. In our case we will only be expanding to the quadrupole moment, that is one step further than Kerr.

This spacetime is given by the following equation in Boyer-Lindquist coordinates:

$$g_{\mu\nu} = -f(dt - \omega d\phi) + \frac{e^{2\gamma}\rho^2}{f\Delta}dr^2 + \frac{e^{2\gamma}\rho^2}{f} + \frac{\Delta\sin^2\theta}{f}d\phi^2 \tag{180}$$

Where analogously to Kerr:

$$\rho^2 = (r - M)^2 - k^2\cos^2\theta \tag{181}$$

$$\Delta = (r - M)^2 - k^2 \tag{182}$$

And f, k, ω and γ are defined by:

$$\alpha = \frac{-M + \sqrt{M^2 - (S/M)^2}}{S/M} \tag{183}$$

$$k = M\frac{1 - \alpha^2}{1 + \alpha^2} \tag{184}$$

$$\beta = q\frac{M^3}{k^3} \tag{185}$$

$$f = e^{2\psi}\frac{A}{B} \tag{186}$$

$$\omega = 2ke^{-2\psi}\frac{C}{A} - 4k\frac{\alpha}{1 - \alpha^2} \tag{187}$$

$$e^{2\gamma} = e^{2\gamma'}\frac{A}{(x^2 - 1)(1 - \alpha^2)^2} \tag{188}$$

$$A = (x^2 - 1)(1 + \mathfrak{ab})^2 - (1 - y^2)(\mathfrak{b} - \mathfrak{a})^2 \tag{189}$$

$$B = \Big((x + 1) + (x - 1)\mathfrak{ab}\Big)^2\Big((1 + y)\mathfrak{a} + (1 - y)\mathfrak{b}\Big) \tag{190}$$

$$C = (x^2 - 1)(1 + \mathfrak{ab})\Big((\mathfrak{b} - \mathfrak{a}) - y(\mathfrak{a} + \mathfrak{b})\Big) + (1 - y^2)(\mathfrak{b} - \mathfrak{a})\Big((1 + \mathfrak{ab}) + x(1 - \mathfrak{ab})\Big) \tag{191}$$

$$\psi = \beta\frac{P_2}{R^3} \tag{192}$$

$$\gamma' = \ln\sqrt{\frac{x^2 - 1}{x^2 - y^2}} + \frac{3\beta^2}{2R^6}(P_3^2 - P_2^2) + \beta\left(-2\sum_{l=0}^{2}\frac{x - y + (-1^{2-l})(x + y)}{R^{l+1}}P_l\right) \tag{193}$$

$$\mathfrak{a} = -\alpha\exp\left(-2\beta\left(-1 + \sum_{l=0}^{2}\frac{(x - y)P_l}{R^{l+1}}\right)\right) \tag{194}$$

$$\mathfrak{b} = \alpha\exp\left(2\beta\left(1 + \sum_{l=0}^{2}\frac{(-1)^{3-l}(x + y)P_l}{R^{l+1}}\right)\right) \tag{195}$$

$$R = \sqrt{x^2 + y^2 - 1} \tag{196}$$

$$P_l = P_l\left(\frac{xy}{R}\right) \tag{197}$$

$$x = \frac{r - M}{k} \tag{198}$$

$$y = \cos\theta \tag{199}$$

Here S is the spin, the unitless spin is given by S/M^2 and q is the quadrupole deviation from the Kerr metric. Here $q < 0$ gives a prolate deviation, and $q > 0$ gives an oblate deviation. This means that when seeing the z direction or the axis of rotation, as vertical, the event horizon gets taller for $q < 0$ and less tall for $q > 0$. This will later be visible when we draw the shadows generated by these spacetimes.
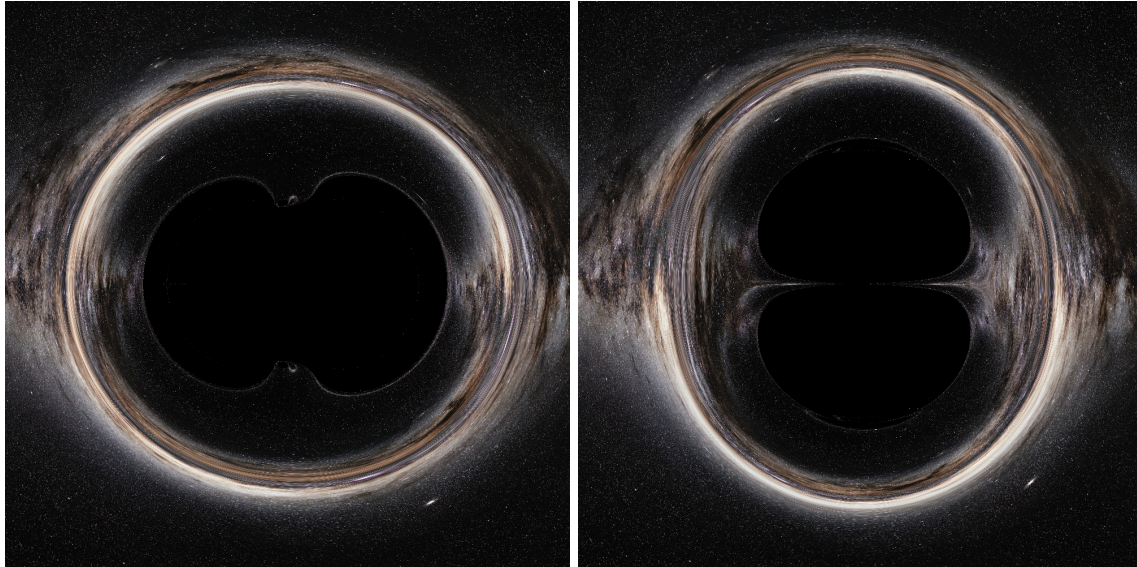
(a) Deviation: $q > 0$ (b) Deviation: $q < 0$

Figure 5: The shadow of a Manko-Novikov black hole for positive and negative deviations from Kerr. Stellar background by: ESO/S. Brunier [Bru]

6   Simulations

In this section I will talk about the numerical methods I use to create simulations of orbits, and images.

6.1   Integrators

The problem of simulation of geodesics in essence boils down to solving a differential equation of the form

$$x' = f(x) \tag{200}$$

Here we want to find the function $x : [t_0, t_n] \to \mathbb{R}^m$. The function $f : \mathbb{R}^m \to \mathbb{R}^m$ and the value $x(t_0)$ is given. To do numerical calculations we split $[t_0, t_n]$ into steps $\{t_0, t_1, ..., t_n\}$ such that $t_{i+1} - t_i = h$ is some small positive number. We now want to find a method that numerically integrates x, that is to say it finds $x(t_{i+1})$ when given $x(t_i)$. There are many methods to do this, in the following sections I will give some examples.

6.1.1   Explicit Euler Integration

The Euler method for solving a differential equation $x' = f(x)$ is based on the idea that for a small enough h:

$$x(t + h) \approx x(t) + hx'(t) \tag{201}$$

This method piecewise linearly approximates x, and thus (assuming x is sufficiently differentiable) it's error is at most of order h^2. We see this because:

$$\lim_{h \to 0} (x(t + h) - x(t) + hx'(t))/h = x'(t) - x'(t) = 0 \tag{202}$$

6.1.2   Runge Kutta Integrators

A Runge-Kutta integrator is in essence a higher order version of Euler. In the way that Eulers method only uses the linear term of the local Taylor expansion of the function, Runge Kutta takes higher order terms into

account as well. The scheme that is used is RK4, or fourth order Runge Kutta. This scheme goes as follows.
Given an equation

$$\frac{dx}{dt} = f(x, t) \tag{203}$$

$$x(t_0) = x_0 \tag{204}$$

We integrate as follows:

$$t_{n+1} = t_n + h \tag{205}$$

$$x_{n+1} = x_n + \frac{1}{6}\left(k_1 + 2k_2 + 2k_3 + k_4\right) \tag{206}$$

where

$$k_1 = f(x_n, t_n) \tag{207}$$

$$k_2 = f(x_n + \tfrac{1}{2}h, t_n + \tfrac{1}{2}hk_1) \tag{208}$$

$$k_3 = f(x_n + \tfrac{1}{2}h, t_n + \tfrac{1}{2}hk_2) \tag{209}$$

$$k_4 = f(x_n + h, t_n + hk_3) \tag{210}$$

$$\tag{211}$$

6.1.3   Symplectic integrators

We also looked into symplectic integrators. These are integrators specifically built for Hamiltonian systems,
usually with the property that they maintain conserved quantities exactly, such as the Hamiltonian. A more
detailed explanation can be found in [Hai10]. Sadly these integrators, while being much more precise, are
not generally explicit. They can be made explicit in some cases, specifically when variables are separable.
An example of this kind of separation would be in the classical Hamiltonian with a potential:

$$H = \frac{p^2}{2m} + V(q) \tag{212}$$

Sadly the variables in our system are not separable, meaning the integration scheme remains implicit. While
this does not entirely prevent us from using them, implicit schemes are significantly more computationally
intensive, and the scheme becoming implicit means that while the conserved quantities remain much more
stable over integration, they are no longer exactly conserved. We therefor decided not to pursue using these
integrators further, and to stick to a simpler integration scheme.

6.2   A comparison

It is of course clear that the RK4 integration scheme is much more computationally intensive per step, but
it is also significantly more precise. For a more complete explanation one can check [**RK4**] (p907). However,
we will also be able to see this difference in precision very clearly in our later simulations. A clear example
of this can be seen in the raytracing we will perform.

6.3   Hardware and software

If we now want to use this simulation of geodesics to create a visual image of a spacetime, such as a picture
of what a black hole would look like, we have another hurdle to overcome. For such an image we can in
essence see every pixel as a ray of light travelling through space. The problem now is that for an image with
a resolution of 1000×1000, to create a sharp image, we need to run our simulation a million times. Since
these simulation are all independent we can try to run them in parallel. To do this we have used the GPU,
the graphical processing unit of the computer. How exactly this works is not necessary knowledge to use
them, the important things to know is that compared to the standard processor of a computer, the GPU
runs slower, but is capable of running a much larger amount of computations in parallel. The restriction is
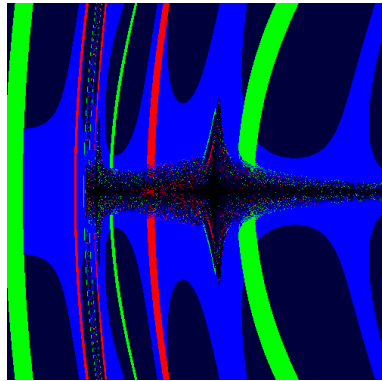
(a) Integrator: RK4
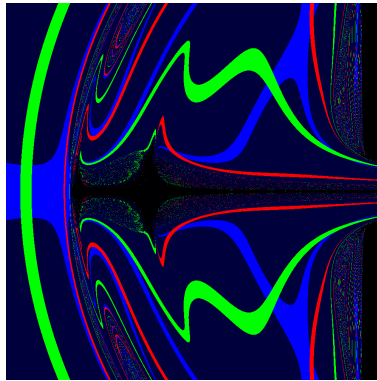
(b) Integrator: Euler
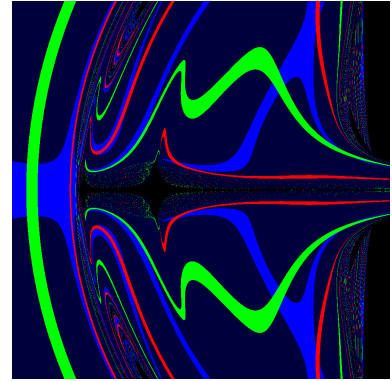
(c) Integrator: Euler, smaller step-size.

Figure 6: Various integrators applied to the raytracing software. The left gives a result much closer to the desired result. Due to symmetry constraints on the system the picture should contain a horizontal blue band. Furthermore the black region in the centre is a calculation error due to a coordinate singularity. We see this get smaller both with stepsize and a better integrator.

however that all these computations need to be the same, but the input of them can be different. For example one can calculate the inner product of millions of pairs of vectors very quickly like this. This calculation was done in python, using the CuPy library, which is an extension of the much used Numpy library. This allows us to distribute an array over the GPU as input.

7   Simulation results

In this section we will discuss the results of the geodesic simulation, this will include singular orbits, images of the shadow and periodic orbits.

7.1   Orbits

First the simulation was run for some simple timelike orbits to try to reconstruct features known from orbits in general relativity spacetimes. In the pictures generated in figure 7 the perihelion precession is seen, which was one of the first experimental proofs of general relativity.
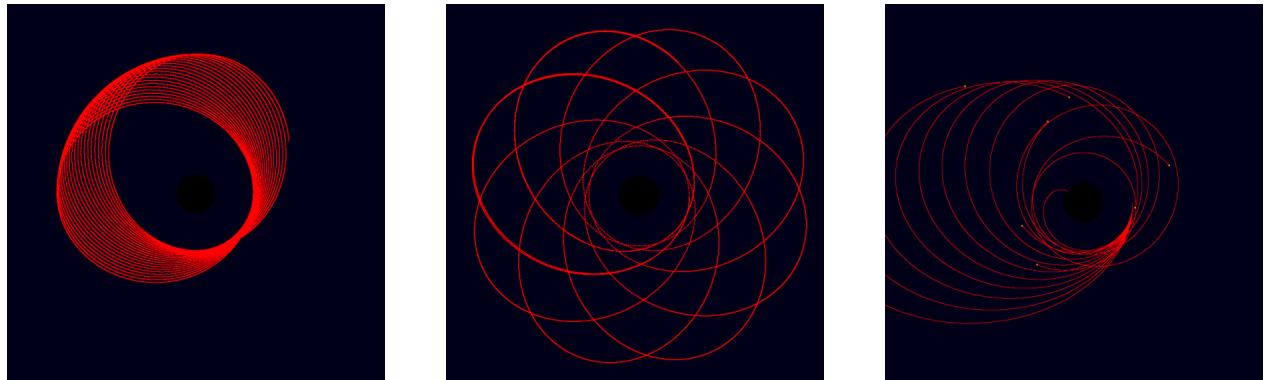
(a)   An   orbit   around   a
Schwarzschild black hole

(b) A resonant orbit around a
Schwarzschild black hole

(c) Multiple orbits run in parallel,
to test performance

Figure 7: Various test orbits run on the simulation program. These are spacelike orbits around the equator of a Schwarzschild black hole.

7.2   The shadow

The second thing the simulation was used for is to render the shadow of black holes, both of Kerr solutions and of Manko Novikov spacetimes. Beside the shadow there are also three lines drawn on the background to see how the curvature lenses it. These lines are drawn at 24 black hole masses from the origin, this is seen in figure 8. The simulation terminates if the cut-off distance is reached, to save calculation time. In a flat space this would give the image seen in figure 9.
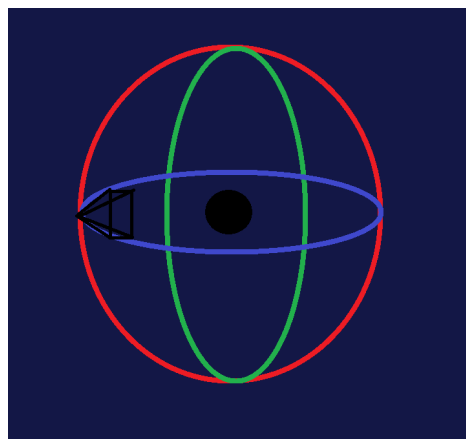

Figure 8: The perspective, dark blue is the background, red green and light blue are lines drawn on a larger sphere around the black hole, the black triangle gives the position of the camera in the sphere.
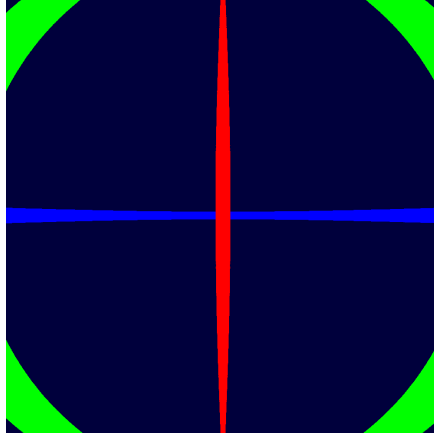
Figure 9: Flat space as seen from the perspective of the camera.

We now draw the shadow of the black hole for some different input parameters. Note that for the Manko Novikov spacetime we cannot set the spin to exactly 0 in the calculation as that leads to division by zero, so in those cases it is set to $S = 0.1M^2$. These images took about 50 minutes each to generate, and have a resolution of 1000×1000 pixels each, they can be seen in figure 12. We see that in the spinless Schwarzschild case the shadow, which is the black part of the image, is exactly round. It is clear from our analysis that the shadow should be a black disk as the system is spherically symmetric, and whether or not a ray falls in is related only to the proportions of it's radial inward momentum compared to it's angular momentum.
We can see that the crossing point of the blue and red lines forms a circle around the shadow, as all these rays get bent around the black hole the same way to end up exactly behind it. We see for Kerr that this circular shape is disturbed, as the rays of light travelling along with the rotation can pass much closer without falling in than those travelling retrograde to it. We can also see secondary echos of the lines in all pictures, which are the rays that travel around the black hole a second time before reaching the background. This is most clear for the red line in the Schwarzschild case. In the Manko-Novikov case we can see that for a deviation below zero we get a taller shadow, and for a deviation larger than zero we get a wider shadow.

(a) $q = -2, S = 0.1M^2$ (b) $q = 0, S = 0.0M^2$ (c) $q = 2, S = 0.1M^2$

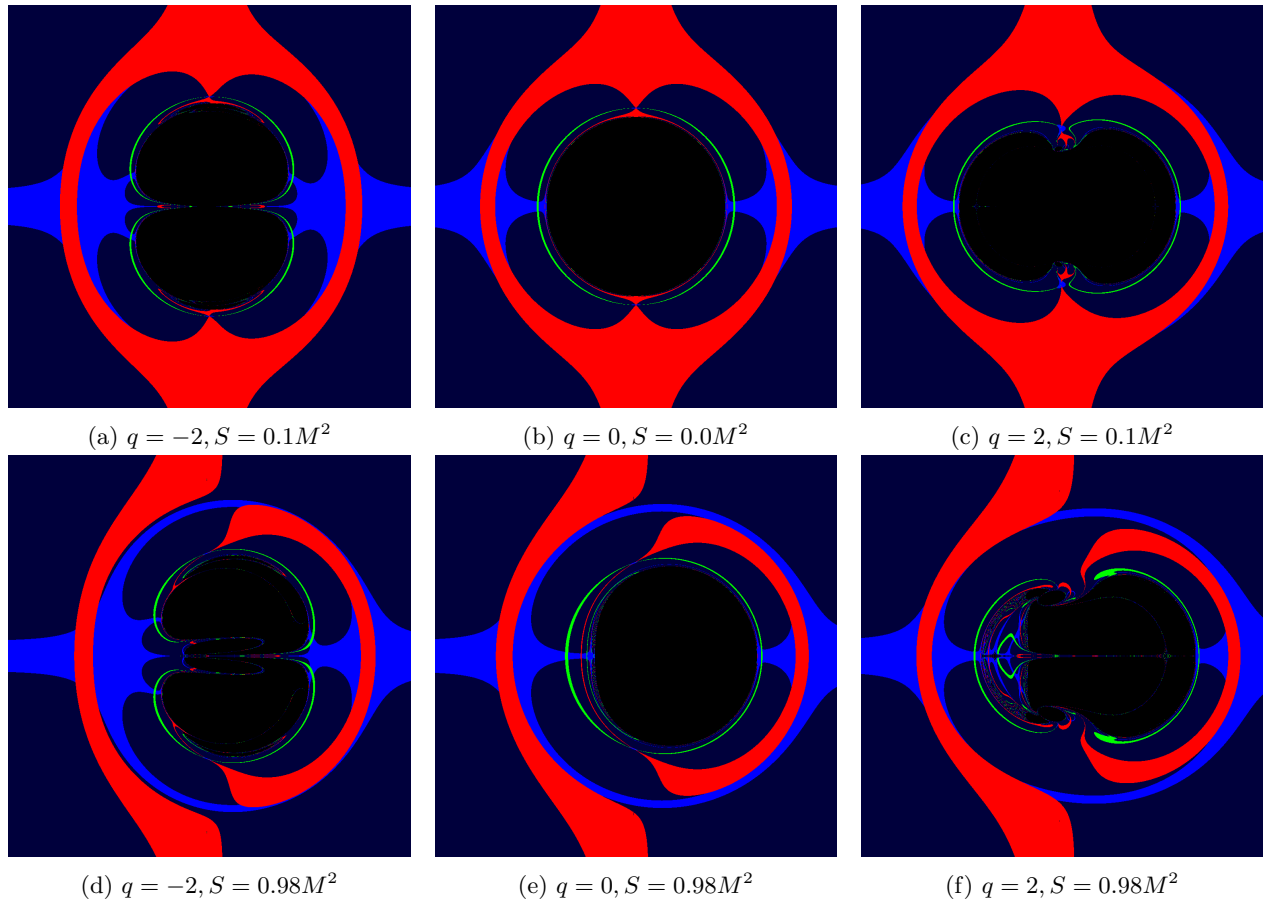(d) $q = -2, S = 0.98M^2$ (e) $q = 0, S = 0.98M^2$ (f) $q = 2, S = 0.98M^2$

Figure 10: Our black hole zoo. We see that as $q > 0$ our shadow becomes more oblate, or wide, whereas as $q < 0$ the shadow becomes more prolate or tall.

Besides the spatial coordinate, we can also gain interesting information from the time coordinate, that is to say, how much (coordinate) time it takes for the light ray to leave the simulations boundary at $r = 24M$. This is plotted in figure 11. The light blue regions in the space plots form the shadow, or the rays that do not leave the bounding box of the simulation before it runs out of steps. We see that in the Manko Novikov case the shadow becomes disconnected, even though the event horizon is a connected whole. Another feature that is a little more visible in this image is that at the equator there seem to be calculation errors.

For now the most interesting of these cases is the high spin $q = 2$ case, as we see some strange chaotic region surrounded by a halo. Rays that exit from this region seem to be following chaotic paths. This is especially visible if one zooms in on the chaotic region in the exit-time plot, seen in figure 13. We sampled a few orbits from this region to see what they would look like, these can be seen in figure 14. The off circular orbits lying at a fixed θ are orbits that hit the event horizon, much like in Kerr they get dragged along the event horizon by the frame dragging. We see in each image that the 9 orbits start very closer together, but diverge quickly once they near the event horizon. This suggests that there might be regions that act as bifurcations of the orbits, or other strange chaotic behaviour.

7.3   Periodic orbits

The orbits that generate the above image, with the halo shaped shadow, give rise to the idea that there might be exotic periodic orbits in the region that those orbits cross. To figure this out the same software was used, but rather than the input values being a spray of orbits originating from a single point of view, the input was a square of rays starting within a range of r and θ values, all with $p_\phi = 1, p_r = p_\theta = 0$. Then the output image was coloured based on the difference between in- and output values for the position and momentum.

(a) $q = -2, a = 0.1$ (b) $q = 0, a = 0.0$ (c) $q = 2, a = 0.1$

(d) $q = -2, a = 0.98$ (e) $q = 0, a = 0.98$ (f) $q = 2, a = 0.98$
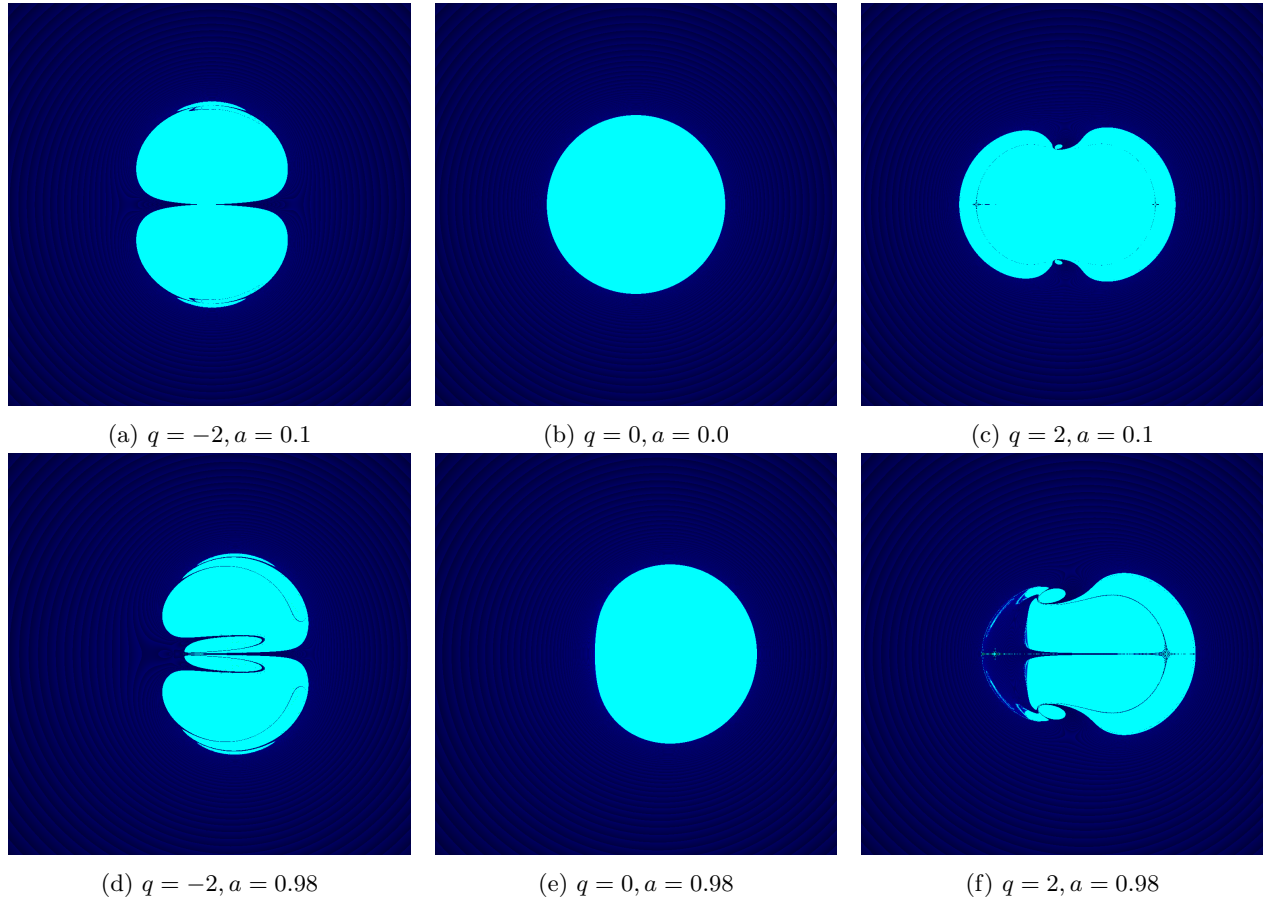
Figure 11: The calculation time for each pixel to reach the exit parameters of the simulation. Cyan is infinity (the simulation did not leave the bounding box before running out of time). Slight banding was added to the gradient to make it easier to see.

We do this first for the Kerr and Schwarzschild spacetimes. This can be seen in figure 15. As we see for Schwarzschild there is a black line of periodic orbits exactly at $r = 3GM$. For the prograde orbits this line curves inward, towards the horizon, as we get closer to the equator where frame-dragging is strongest. Conversely for the retrograde orbits the line of periodic orbits curve outwards, as frame-dragging hinders them instead of propelling them. The yellow line in retrograde orbits lies at the inner horizon. We see in the Kerr case there are some red pixels in the dark area. This is due to the periodic orbits not necessarily being periodic in a single rotation of ϕ. Orbits may be periodic over multiple rotations of ϕ, or even be pseudo-periodic, that is to say they never fall into the black hole or fly off to infinity, but never return to their exact starting position. In fact, given any distance, they will at some point come closer than that distance to the starting point, but they will never reach it.

The separation is easier to see in figure 16, where the pixels are separated into two groups. Orbits denoted by red pixels fly out to infinity while orbits denoted by black pixels fall into the black hole.

We can create the same plots for the Manko-Novikov spacetime where we slowly increase the quadrupole deviation from 0.01 to the 2 we have in the case with the halo shaped shadow. We see these in figure 17 and figure 18. The pictures with two regions are generated as such that all orbits that increase in radius past a distance of $4M$ are considered as leaving orbits, and those that stay inside this are considered as falling in. This is of course a very imprecise method of looking for these orbits, however especially for Kerr and Schwarzschild spacetimes this is accurate enough, as most orbits that leave tend to do so fairly quickly. Furthermore orbits that take multiple rotations to leave are often close to orbits that are periodic.

For a higher precision we can increase the amount of orbits before the simulation is stopped, at the cost of

increasing the calculation time linearly with the amount of orbits. This is seen in figure 19. We see that much more structure appears, as more orbits that didn't leave in a single rotation leave the bounded region. We see a fractal-like pattern appear with strands of orbits that fall in woven inbetween those that leave, which suggests a very rich and chaotic structure in the geodesics. The parallel curvesin this picture seem to be related to the concentric circles and parallel curves seen in the shadow in figure 13.

Some of these orbits can be seen in figure 20, again each picture contains 9 orbits starting with slightly varied positions. We see that especially near the equator, strange behaviour occurs with geodesics getting deflected. Beyond that some orbits look like those of Kerr black holes, drawing out parts of a torus, however again near the equator these orbits tend to have strange bends in them. The most interesting behaviour is the diverging-converging behaviour of the different orbits, this is especially clear in the bottom left picture, where as the rays near the equator they diverge, but as they leave the equatorial area they will converge again. This behaviour suggests at least some measure of stability in these periodic orbits. It is however very difficult to state anything about true stability of these orbits without analysing the Poisson return-maps of these orbits, which the software cannot yet do.

8   Further Analysis of Numerical Results

In the previous section we have numerically evaluated both the shadows and the periodic orbits of various spacetimes. We have compared these simulations to the analytical calculations we did for the Schwarzschild spacetime and saw that they indeed aligned. We can compare the shadows projected by Manko-Novikov black holes like in figure 13 to the visual images created by the Event Horizon Telescope, as seen in figure 21. We can see that the exotic case deviates rather strongly from the observations. It is clear that the parameters we chose for our black holes lie rather on the extreme end, and while we cannot immediately conclude that the solution does not describe the observed black hole, we have some loose boundaries on our parameters.

As we can see in figure 19 that the lightlike orbits of the Manko-Novikov space have a very detailed structure. In figures 20 we saw some examples, we can see by their converging-diverging behaviour that there seems to be some form of stability in these orbits. To further analyse this stability mathematically we would want to calculate Poincaré return maps. A Poincaré return map is a map generated by taking a surface around a periodic orbit, and watching how the points on the surface move around after allowing them to travel along the flow for one rotation. For a more rigorous treatment of these return maps one can read the textbook by McDuff and Salamon [D M98]. If we linearise this returnmap at the periodic orbit we get a linear map from a vectorspace, the tangentspace of the transversal surface, to itself. We can calculate the eigenvalues of this map, these are called the Floquet multipliers. An important result about these returnmaps states that these are independent of the chosen surface, again for the proof we refer to [D M98]. These multipliers give direct quantitative information about the stability of the orbit. If a multiplier λ has $|\lambda| < 1$ the orbit is stable or attractive in that direction. If it has $|\lambda| = 1$ then either there are more periodic orbits in that direction, or the stability of the point is degenerate. In the case of Schwarzschild for instance we would have multipliers larger than 1 in the r and p_r directions, as the orbits are unstable, while in the θ and p_θ direction we would have multipliers of 1, as there are more periodic orbits in that direction on the photon sphere.

Sadly we were not able to fully analyse the periodic orbits and their returnmaps to verify this stability. This was because the straight forward way of calculating this map would require knowing the exact values of the periodic orbit. We attempted methods that would allow fitting higher dimensional parabolas to extract the Floquet multipliers from their parameters, however the project ran out of time before we were able to fully implement this.

Should we be able to calculate these values though, we would be able to take some conclusions about the spacetime. Were the orbits to be fully stable however the spacetime itself runs into instability. Because these stable orbits will accumulate mass over time they will disrupt the spacetime, as it will no longer be a vaccuum solution. How exactly this will work is unclear, it is possible that this behaviour will radiate off the extra multipole moments, turning the spacetime back into Kerr, or it is possible a new strange spacetime will be born. It is unclear what will happen without further full numerical relativity simulations.

9 Discussion and Outlook

Our goal was to improve the attainable resolution of black-hole shadows, and to look for periodic orbits. To do this we have first looked at the mathematics behind the dynamics of geodesics. We have seen from this that in Schwarzschild case we can fully reduce our problem to only the radius variable. Symplectic reduction is a powerful extension of Noethers theorem, which allows one to remove dimensions from the system, using the conserved quantity. This reduction in dimension is a useful tool for physical analysis, as it allows for much easier intuition about the system. From our calculations on the dynamics of rays of light in a Schwarzschild spacetime we were able to find exactly what periodic orbits existed, and what the expected shape of the shadow should be. We then used this to compare to our numerics, which showed the expected result. To be able to execute the numerical calculations on a personal computer rather than a computing cluster we made use of a graphical processing library for python. This allowed us to increase the resolution to modern standards without calculations taking multiple hours.

We used symplectic geometry to fully reduce the Schwarzschild case to only a single coordinate and momentum. To do this we first applied Noethers and extensions of Marsden-Weinsteins theorem to the symmetries of the spacetime. We were able to make intuitive statements about both the shape of the shadow and the periodic orbits of the spacetime from this analysis. We used this to verify the numerical results in the Schwarzschild case we expanded the numerical simulation to the Kerr spacetime, where we could compare to analytical calculations in literature , such as [CF 16], and we see that indeed the shadow became lobsided in the way that was expected. Similarly we found that the periodic and pseudo-periodic orbits were located on surfaces that were either closer to the horizon for rays travelling along with the spin, and further away for for those travelling against the rotation. With these two surfaces meeting at the poles of the black hole.

After using the numerical simulation to draw the shadow and periodic orbits of Kerr we expanded to a much more exotic type of black hole. The Manko-Novikov spacetime has extra mass-multipole moments compared to Kerr. This spacetime violates the no-hair conjecture which states that the only properties that define a black hole are mass, spin and electromagnetic charge. Furthermore it partially violates the cosmic censorship conjecture, which states that a singularity must be hidden by an event horizon, it has a curvature singularity which lies on the equator of the spheroidal event horizon. It is however a fully analytical solution of Einsteins equations for the theory of general relativity, and therefor an interesting object of study to test these conjectures. For our simulations we looked only at the first parameter of deviation from Kerr, the quadrupole moment of the Manko-Novikov black hole. We see that these deviations affect the shape of the shadow drastically, making the shadow taller or wider from the equatorial point of view. We also see that especially in the positive deviations, strange behaviours occur in both the shadow, and singular geodescics. We can compare our findings to those by [M W18]. We see that using the GPU-accelerated processing we were able to significantly increase resolution, and also the precision. This increase in precision was despite the integrator we used being a basic RK-4, compared to the RK-5 integrator they used, which corrected for conserved quantities. This increase in precision is most noticable in the shadows with high deviation from Kerr, where certain regions that seem to be chaotic at first resolve as the precision increases. This is clearest in the high spin case with $q = 2$.

We used the same numerical software to look for periodic orbits of the Manko-Novikov spacetime. We saw many of the same features that were in the shadow arise also in the periodic orbits, most notably the parallel curves seen in figure 19. We also analysed We attempted to use Poincaré return maps and their eigenvalues called Floquet multiplies to numerically evaluate the stability of periodic orbits. This would give strong indications about the stability of the solutions. If orbits were to be fully stable they would accumulate energy over time and disrupt the spacetime, meaning that the black hole in the exact Manko-Novikov form will be shortlived.

We can compare our rendered shadows of the Manko-Novikov spacetime to the image in figure 21 by the Event Horizon Telescope collaboration. It is hard to make rigorous statements about whether or not this black hole is of Manko-Novikov type. This is due to both the resolution of the observation and the extreme deviation parameters we used. For a more accurate comparison many things could be done in future research. Future versions of the code we used should be able to generate off equator points of view of the Kerr black hole. We did not do this in this version to reduce calculation time by a factor 2, since there is an equatorial symmetry in the system. Furthermore future research would be able to add objects around the black hole such as the accretion disk, similar to that visible in the picture of the Messier-87 black hole. Other possible

objects to add around the black hole would be orbiting stars, to determine how their orbits would be observed after lensing. This would allow one to use the distorted shapes and paths of these stars as seen by a far-away observer to calculate the mass and spin of a black hole, and possibly deviation parameters such as those of a Manko-Novikov black hole. This is similar to how the black hole in the centre of the galaxy was discovered in [Ghe+98].

So to conclude we have significantly increased the precision and speed attainable in calculations on shadows and periodic orbits of black-hole solutions. We did this using both symplectic geometry and theory about integrators. Future works could use this increase in performance to explore more of the parameter space of Manko-Novikov, or for quicker results in research into more classical black hole solutions.

A   Python Scripts

A.1   Code for propagation of rays

```
#prerequisites:
#Visual studio 2019.
#CUDA 11.5 (note, earlier versions might work, 11.6 definitely does not).
#Both NumPy and CuPy libraries, CUPY requires the two above.
#Pillow for exporting an image

#in general variables starting with 'the/loc' are local in the function/loop, whereas 'glob

import sys
import math
import numpy as np
import cupy as cp
import time
from PIL import Image

#The three constants that define our black hole
globalM = 0.5
globalS = 0.24
globalQ = 2.0

#Image resolution and field of view for raytracing

resX = 1000
resY = 1000
#resY must be even
screenResolution = (resX,resY)
globalFOV = 75.0


#function that defines the metric, it automatically uses the global constants defined for u
def metricMatrixNP(theCoord,locM = globalM, locS = globalS, locQ = globalQ):

    theMetricArray = [[0,0,0,0],[0,0,0,0],[0,0,0,0],[0,0,0,0]]

    #Here goes formulas to define the metric

    return(theMetricArray)

#Chooses the t component of a vector so that it is lightlike (note that a − sign change mi
def lightlikeT(theSpaceQdot, theCoord ,theM = globalM, theS = globalS, theQ = globalQ):
    theMatrix = metricMatrixNP(theCoord,theM, theS,theQ)
    tempA = theMatrix[0][0]
    tempB = 0
    for i in range(3):
        tempB = tempB + theSpaceQdot[i]*theMatrix[0][i+1]*2.0
    tempC = 0
    for i in range(3):
        for j in range(3):
            tempC = tempC + theSpaceQdot[i]*theMatrix[i+1][j+1]*theSpaceQdot[j]
    theTQdot = (−tempB + np.sqrt(tempB*tempB − 4.0*tempA*tempC))/(2.0*tempA)
```

```
    return(theTQdot)
```

```
#The real calculation. Note that once data is sent to the GPU there is no more communicatio
#No constants from "outside" can be used or altered in any way. The only data the GPU knows
#The method used for geodesics is Hamiltonian. As follows:
#\partial_\tau q^\mu = g^{\mu\nu} p_\nu
#\partial_\tau p_\mu = \partial_\mu g^{\nu\sigma} p_\nu p_\sigma
#Here upper indices act as vectors, lower indices act as covectors, such as the momentum
#g^{\mu\nu} is given by theMetricArray[\mu][\nu]
#\partial_\mu g^{\nu\sigma} is given by theDerMetricArray[\mu][\nu][\sigma]
#Timesteps are normalized by \dot{q_t} so that the simulation is in coordinate time.
#A cutoff is made once the timestep reaches a certain threshold, this is considered reachin
#A cutoff is also made if q_r, the radius, reaches 1.5 times the starting radius. This is
#In the end only the end position of the input geodesic is returned

geodesicKernel = cp.ElementwiseKernel(
    'float32 theT, float32 theR, float32 theTheta, float32 thePhi, float32 thePT, float32 th
    'float32 theEndT, float32 theEndR, float32 theEndTheta, float32 theEndPhi',
    ''',

//Variable initialisation, code within this kernel is not in python, it is in C
double theQ[4] = {theT, theR, theTheta, thePhi};
double theP[4] = {thePT, thePR, thePTheta, thePPhi};
double theR0 = 1.5*theR;

double derPrecision = 0.00000001;
double stepPrecision = 0.00015;

double Metric[4][4] = {{0,0,0,0},{0,0,0,0},{0,0,0,0},{0,0,0,0}};
double dRMetric[4][4] = {{0,0,0,0},{0,0,0,0},{0,0,0,0},{0,0,0,0}};
double dThetaMetric[4][4] = {{0,0,0,0},{0,0,0,0},{0,0,0,0},{0,0,0,0}};
double DerMetric[4][4][4] = {{{0,0,0,0},{0,0,0,0},{0,0,0,0},{0,0,0,0}},{{0,0,0,0},{0,0,0,0}

double theDeltaP1[4] = {0,0,0,0};
double theDeltaQ1[4] = {0,0,0,0};
double theDeltaP2[4] = {0,0,0,0};
double theDeltaQ2[4] = {0,0,0,0};
double theDeltaP3[4] = {0,0,0,0};
double theDeltaQ3[4] = {0,0,0,0};
double theDeltaP4[4] = {0,0,0,0};
double theDeltaQ4[4] = {0,0,0,0};

//The RK4 integrator in a loop
for (int i = 0 ; i < theN ; i++) {

//———————————————————— K1
    metricAtPoint(Metric, theQ[1], theQ[2], locM, locS, locVarQ);
    metricAtPoint(dRMetric, theQ[1] + derPrecision, theQ[2], locM, locS, locVarQ);
    metricAtPoint(dThetaMetric, theQ[1], theQ[2] + derPrecision, locM, locS, locVarQ);

    for(int mu = 0 ; mu < 4 ; mu++) {
    for(int nu = 0 ; nu < 4 ; nu++) {
        DerMetric[1][mu][nu] = (dRMetric[mu][nu] − Metric[mu][nu])/derPrecision;
```

```
        DerMetric [2][mu][nu] = (dThetaMetric [mu][nu] − Metric [mu][nu])/derPrecision ;
    };
    };

    for (int mu = 0 ; mu < 4 ; mu++) {
        theDeltaP1 [mu] = 0;
    for (int nu = 0 ; nu < 4 ; nu++) {
    for (int sigma = 0 ; sigma < 4 ; sigma++) {
        theDeltaP1 [mu]+= −0.5∗DerMetric [mu][nu][sigma]∗theP [nu]∗theP [sigma];
    };
    };
    };

    for (int mu = 0 ; mu < 4 ; mu++) {
        theDeltaQ1 [mu] = 0;
    for (int nu = 0 ; nu < 4 ; nu++) {
        theDeltaQ1 [mu]+= Metric [mu][nu]∗theP [nu];
    };
    };

    double timeScale = abs (stepPrecision/theDeltaQ1 [0]); //not sure what to do here , just u

//————————————————— K2
    metricAtPoint (Metric , theQ [1]+0.5∗timeScale∗theDeltaQ1 [1], theQ [2]+0.5∗timeScale∗theDelta
    metricAtPoint (dRMetric , theQ [1]+0.5∗timeScale∗theDeltaQ1 [1] + derPrecision , theQ [2]+0.5∗
    metricAtPoint (dThetaMetric , theQ [1]+0.5∗timeScale∗theDeltaQ1 [1], theQ [2]+0.5∗timeScale∗th

    for (int mu = 0 ; mu < 4 ; mu++) {
    for (int nu = 0 ; nu < 4 ; nu++) {
        DerMetric [1][mu][nu] = (dRMetric [mu][nu] − Metric [mu][nu])/derPrecision ;
        DerMetric [2][mu][nu] = (dThetaMetric [mu][nu] − Metric [mu][nu])/derPrecision ;
    };
    };

    for (int mu = 0 ; mu < 4 ; mu++) {
        theDeltaP2 [mu] = 0;
    for (int nu = 0 ; nu < 4 ; nu++) {
    for (int sigma = 0 ; sigma < 4 ; sigma++) {
        theDeltaP2 [mu]+= −0.5∗DerMetric [mu][nu][sigma]∗(theP [nu]+0.5∗timeScale∗theDeltaP1 [n
    };
    };
    };

    for (int mu = 0 ; mu < 4 ; mu++) {
        theDeltaQ2 [mu] = 0;
    for (int nu = 0 ; nu < 4 ; nu++) {
        theDeltaQ2 [mu]+= Metric [mu][nu]∗(theP [nu]+0.5∗timeScale∗theDeltaP1 [nu]);
    };
    };

//————————————————— K3
    metricAtPoint (Metric , theQ [1]+0.5∗timeScale∗theDeltaQ2 [1], theQ [2]+0.5∗timeScale∗theDelta
    metricAtPoint (dRMetric , theQ [1]+0.5∗timeScale∗theDeltaQ2 [1] + derPrecision , theQ [2]+0.5∗
    metricAtPoint (dThetaMetric , theQ [1]+0.5∗timeScale∗theDeltaQ2 [1], theQ [2]+0.5∗timeScale∗th
```

```
    for ( int  mu  =  0  ;  mu  <  4  ;  mu++) {
    for ( int  nu  =  0  ;  nu  <  4  ;  nu++) {
        DerMetric [1][mu][ nu]  =  (dRMetric [mu][nu]  −  Metric [mu][nu])/derPrecision ;
        DerMetric [2][mu][ nu]  =  (dThetaMetric [mu][nu]  −  Metric [mu][nu])/derPrecision ;
    };
    };


    for ( int  mu  =  0  ;  mu  <  4  ;  mu++) {
        theDeltaP3 [mu]  =  0;
    for ( int  nu  =  0  ;  nu  <  4  ;  nu++) {
    for ( int  sigma  =  0  ;  sigma  <  4  ;  sigma++) {
        theDeltaP3 [mu]+=  −0.5∗DerMetric [mu][nu][ sigma]∗(theP [nu]+0.5∗timeScale∗theDeltaP2 [n
    };
    };
    };


    for ( int  mu  =  0  ;  mu  <  4  ;  mu++) {
        theDeltaQ3 [mu]  =  0;
    for ( int  nu  =  0  ;  nu  <  4  ;  nu++) {
        theDeltaQ3 [mu]+=  Metric [mu][nu]∗(theP [nu]+0.5∗timeScale∗theDeltaP2 [nu]);
    };
    };
```

//————————————————— K4
```
    metricAtPoint ( Metric , theQ [1]+timeScale∗theDeltaQ3 [1] , theQ [2]+ timeScale∗theDeltaQ3 [2] , lo
    metricAtPoint (dRMetric , theQ [1]+timeScale∗theDeltaQ3 [1]  +  derPrecision , theQ [2]+ timeScale
    metricAtPoint (dThetaMetric , theQ [1]+timeScale∗theDeltaQ3 [1] , theQ [2]+ timeScale∗theDeltaQ3

    for ( int  mu  =  0  ;  mu  <  4  ;  mu++) {
    for ( int  nu  =  0  ;  nu  <  4  ;  nu++) {
        DerMetric [1][mu][ nu]  =  (dRMetric [mu][nu]  −  Metric [mu][nu])/derPrecision ;
        DerMetric [2][mu][ nu]  =  (dThetaMetric [mu][nu]  −  Metric [mu][nu])/derPrecision ;
    };
    };


    for ( int  mu  =  0  ;  mu  <  4  ;  mu++) {
        theDeltaP4 [mu]  =  0;
    for ( int  nu  =  0  ;  nu  <  4  ;  nu++) {
    for ( int  sigma  =  0  ;  sigma  <  4  ;  sigma++) {
        theDeltaP4 [mu]+=  −0.5∗DerMetric [mu][nu][ sigma]∗(theP [nu]+timeScale∗theDeltaP3 [nu])∗
    };
    };
    };


    for ( int  mu  =  0  ;  mu  <  4  ;  mu++) {
        theDeltaQ4 [mu]  =  0;
    for ( int  nu  =  0  ;  nu  <  4  ;  nu++) {
        theDeltaQ4 [mu]+=  Metric [mu][nu]∗(theP [nu]+timeScale∗theDeltaP3 [nu]);
    };
    };



    //————————————Adding  final  positions
```

```
        for(int mu = 0 ; mu < 4 ; mu++) {
            theP[mu] += timeScale*0.1667*(theDeltaP1[mu] + 2*theDeltaP2[mu] + 2*theDeltaP3[mu]
            theQ[mu] += timeScale*0.1667*(theDeltaQ1[mu] + 2*theDeltaQ2[mu] + 2*theDeltaQ3[mu]
        };

        //Gives exit parameters, in this case a maximum radius and minimum timestep
        if(theQ[1] > theR0) break;
        if(timeScale < stepPrecision*0.00003) break;
    };

    #Saves the end positions to the return variables
    theEndT = theQ[0];
    theEndR = theQ[1];
    theEndTheta = theQ[2];
    theEndPhi = theQ[3];
        ''',
        'geodesic',
        preamble='''
    __device__ void metricAtPoint(double ioMetric[4][4], double locR, double locTheta, double l
    {

        //Here goes formulas to define the INVERSE metric

        ioMetric[0][0] = -1/locF + locF*locOmega*locOmega/(locDelta*locSinTheta*locSinTheta);
        ioMetric[1][1] = locF*locDelta/(locExpGamma*locRho2);
        ioMetric[2][2] = locF/(locExpGamma*locRho2);
        ioMetric[3][3] = locF/(locDelta*locSinTheta*locSinTheta);
        ioMetric[0][3] = locF*locOmega/(locDelta*locSinTheta*locSinTheta);
        ioMetric[3][0] = ioMetric[0][3];
    };
        ''')

    #The below kernel simply turns output positions into colours. Large R becomes blue, small R

    colourKernel = cp.ElementwiseKernel(
        'float32 theT, float32 theR, float32 theTheta, float32 thePhi',
        'int32 colors',
        '''
        float theQ[4] = {theT, theR, theTheta, thePhi};
    if (theQ[1] > 8.0) {
        if (__sinf(theQ[3])*__sinf(theQ[3]) < 0.01) {
            colors = 0xff0000ff;
        } else if (__cosf(theQ[3])*__cosf(theQ[3]) < 0.01) {
            colors = 0xff00ff00;
        } else if (__sinf(2.0*theQ[2])*__sinf(2.0*theQ[2]) < 0.01) {
            colors = 0xffff0000;
        } else {
            colors = 0xff3c0000;
        }
    //} else if (theQ[1] > 5.0*0.5) {
    //        colors = 0xff00ff00;
    } else {
        colors = 0xff000000;
    }    ''',
```

```
    'colours')


start_time = time.time()
print("initializing_positions")


#The position from which we view
globQ0 = [0.0,8.0,cp.pi*0.5,0.0]

#The position from which we view, but as an array of resX times resY times the same positio
globT0 = cp.ones(screenResolution,dtype=cp.float32)*globQ0[0]
globR0 = cp.ones(screenResolution,dtype=cp.float32)*globQ0[1]
globTheta0 = cp.ones(screenResolution,dtype=cp.float32)*globQ0[2]
globPhi0 = cp.ones(screenResolution,dtype=cp.float32)*globQ0[3]

#Calculating the correct horizontal and vertical field of view, usually just the same, but
verticalRange = np.tan(0.5*globalFOV/180*np.pi)/globQ0[1]
horizontalRange = np.arctan(np.tan(verticalRange)*resX/resY)

#The starting direction of our rays, in essence a rasterized screen in the tangent space o
pr = cp.ones(screenResolution,dtype=cp.float32)*-1.0
pphiPREMESH = cp.linspace(-horizontalRange,horizontalRange,screenResolution[0],dtype=cp.flo
pthetapphiPREMESH = cp.linspace(-verticalRange,verticalRange,screenResolution[1],dtype=cp.f
ptheta, pphi = cp.meshgrid(pthetapphiPREMESH,pphiPREMESH)

#Getting the correct \dot{q_t} to be lightlike
pt = lightlikeT([pr,ptheta,pphi],globQ0,globalM,globalS,globalQ)

#Turning starting directions into starting momenta (which are covectors)
curvatureQ0 = metricMatrixNP(globQ0,globalM,globalS,globalQ)

globPT0 = pt*curvatureQ0[0][0] + pr*curvatureQ0[0][1] + ptheta*curvatureQ0[0][2] + pphi*cur
globPR0 = pt*curvatureQ0[1][0] + pr*curvatureQ0[1][1] + ptheta*curvatureQ0[1][2] + pphi*cur
globPTheta0 = pt*curvatureQ0[2][0] + pr*curvatureQ0[2][1] + ptheta*curvatureQ0[2][2] + pph
globPPhi0 = pt*curvatureQ0[3][0] + pr*curvatureQ0[3][1] + ptheta*curvatureQ0[3][2] + pphi*c

#the constants, which also need to be given to the GPU per core
globalML = cp.float32(globalM)
globalSL = cp.float32(globalS)
globalQL = cp.float32(globalQ)

print(time.time()-start_time)
start_time = time.time()
print("beginning_GPU_calculation")

#The actual calculation. The input is 8 cupy arrays of the exact same shape (resX times res
Tboard,Rboard,ThetaBoard,PhiBoard = geodesicKernel(globT0,globR0,globTheta0,globPhi0,globPT
cp.cuda.Stream.null.synchronize()

#Saving the out positions as 4 numpy arrays, for further analysis without re-running an ho
np.save("outputTBoard.npy",Tboard)
np.save("outputRBoard.npy",Rboard)
np.save("outputThetaBoard.npy",ThetaBoard)
np.save("outputPhiBoard.npy",PhiBoard)
```

```python
#Turning the output positions into a bmp
colourBoard = np.transpose(colourKernel(Tboard,Rboard,ThetaBoard,PhiBoard))
cp.cuda.Stream.null.synchronize()

print(time.time()-start_time)
start_time = time.time()
print("beginning drawing")

#Turning out array back to numpy to be able to draw it
colourBoardNP = cp.asnumpy(colourBoard)

#Saves the array as an image
rgb_img = im = Image.fromarray(colourBoardNP, 'RGBA')
rgb_img.save('image.png')

print(time.time()-start_time)
```
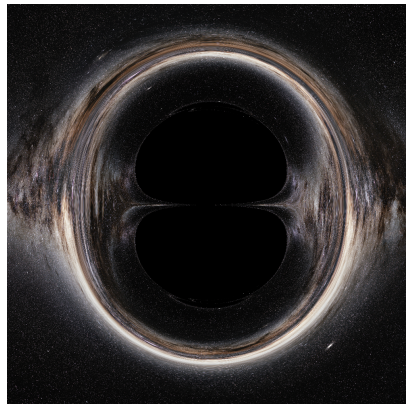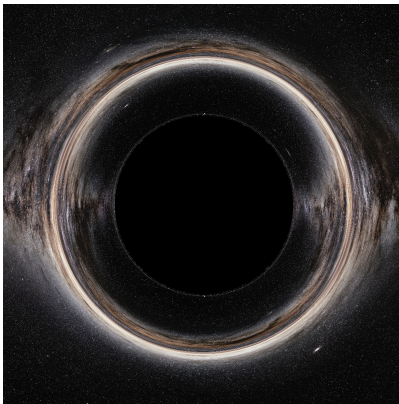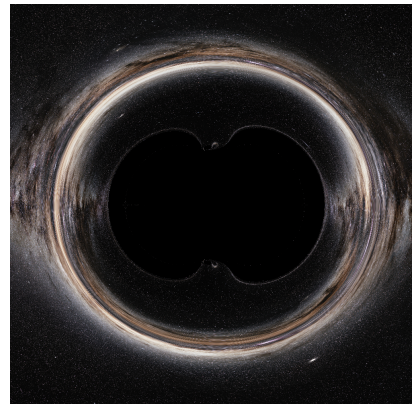
(a) Milky Way panorama by [Bru], to provide a more realistic background.

(b) $q = -2, a = 0.1$

(c) $q = 0, a = 0.0$

(d) $q = 2, a = 0.1$
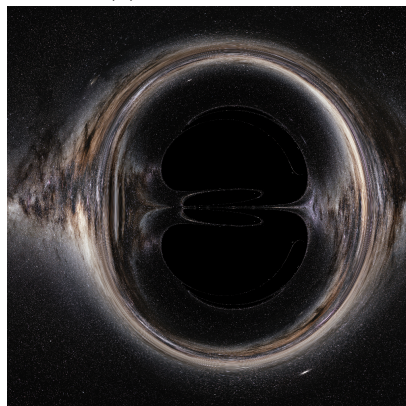
(e) $q = -2, a = 0.98$
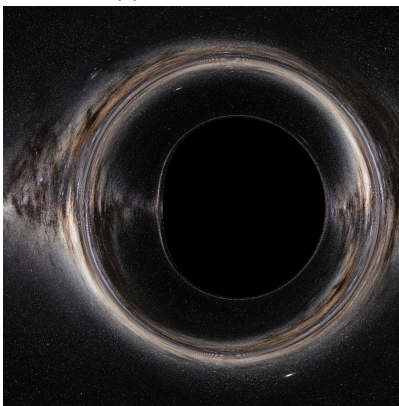
(f) $q = 0, a = 0.98$
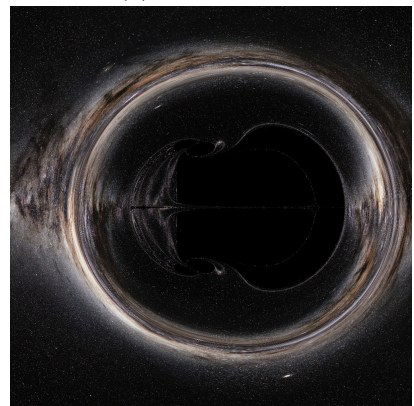
(g) $q = 2, a = 0.98$

Figure 12: For these images the three lines on the background were replaced with a texture. Bilinear texture filtering was used to make the image look less pixelated.
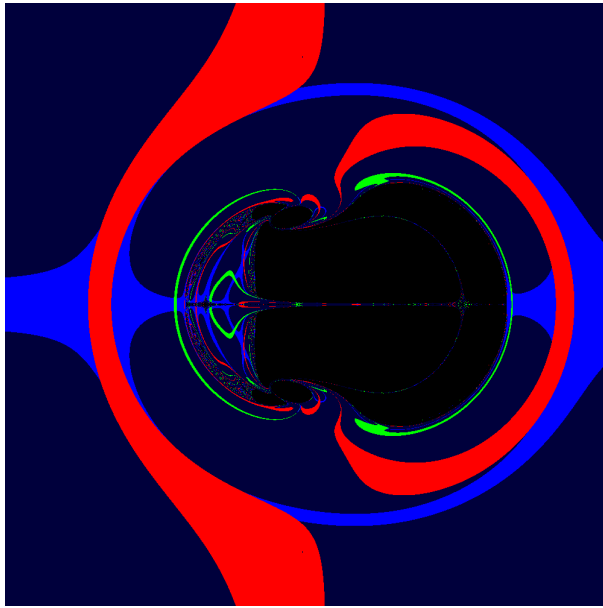
(a) $q = 2, a = 0.98M$ spatial render.
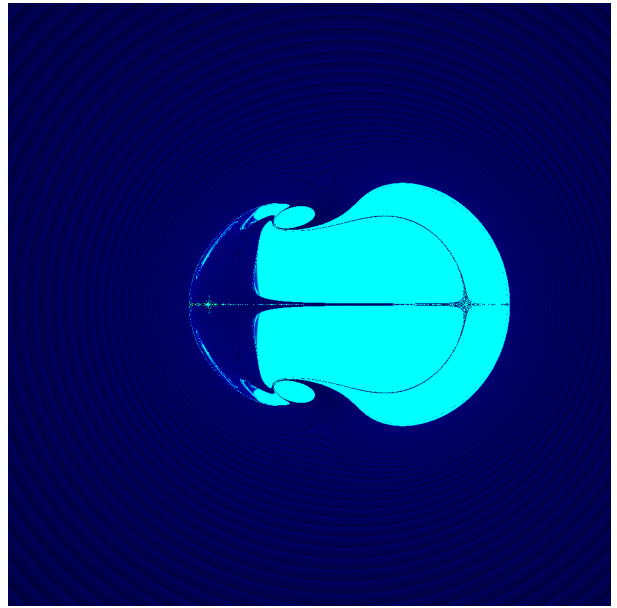
(b) $q = 2, a = 0.98M$ exit time.
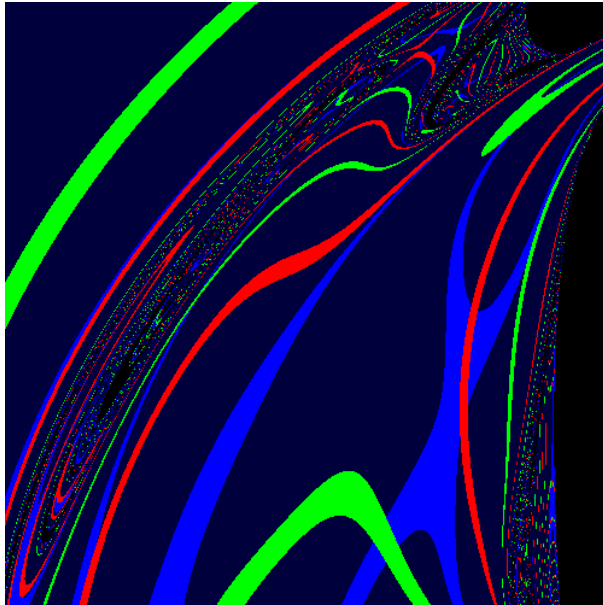
(c) $q = 2, a = 0.98M$ spatial render, zoomed in.
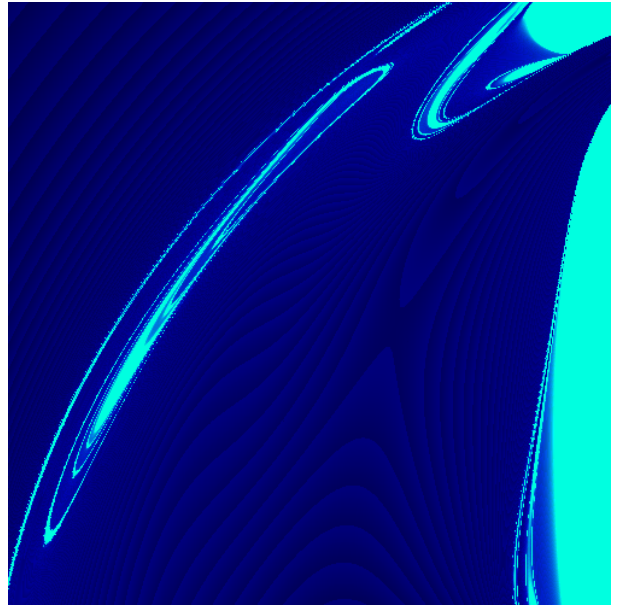
(d) $q = 2, a = 0.98M$ exit time, zoomed in.

Figure 13: A render of the Manko Novikov, zoomed in on the area enclosed by the Halo above the horizon. In the bottom left picture we see that this region deflects rays very chaotically, as all colours are present meaning rays get deflected in every direction. In the bottom right we see that there is an extra part of the shadow, disconnected from the rest of the structure, which seems to be shaped like concentric rings, or a similar shape.
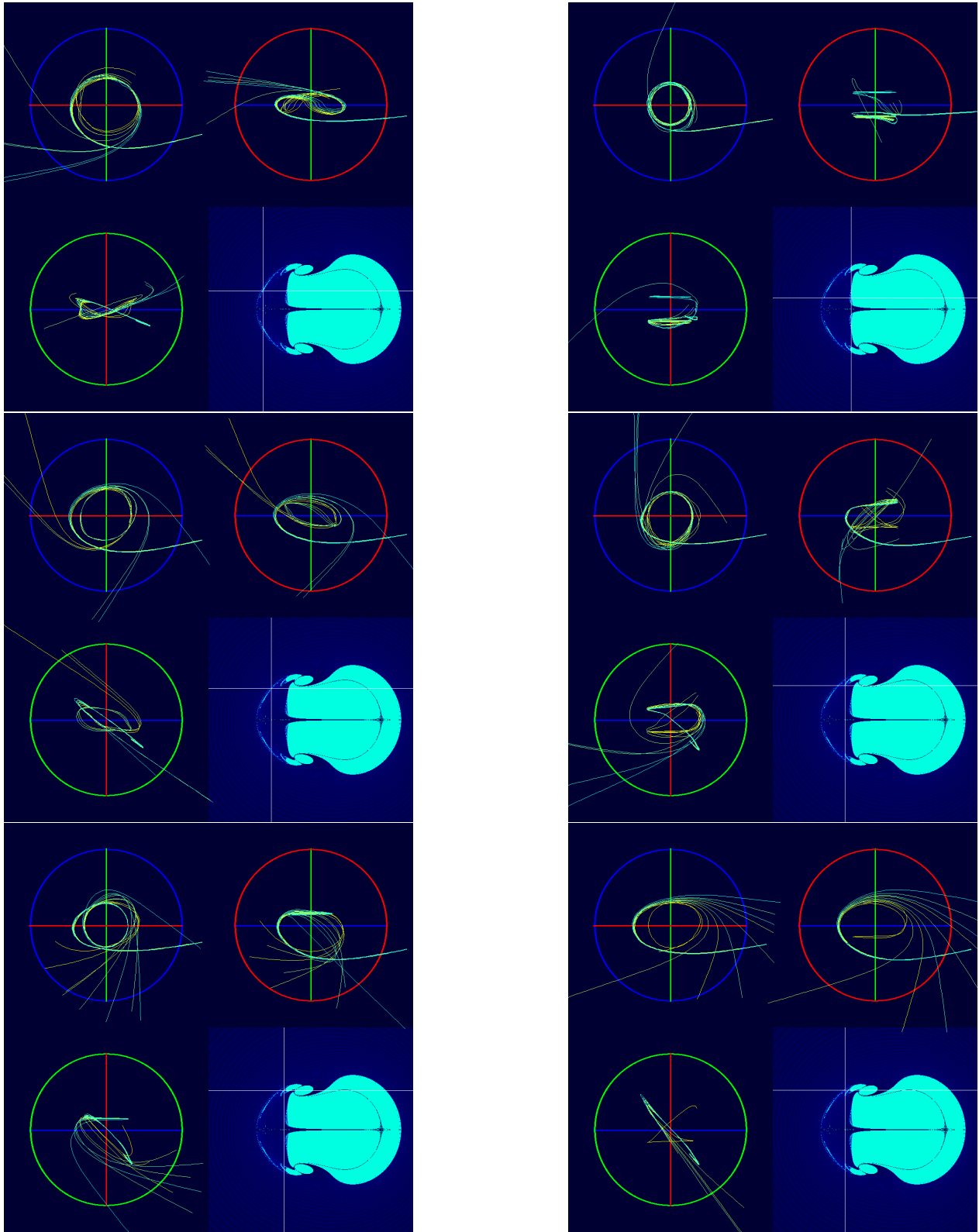
Figure 14: Samples of orbits from the generated shadows of the Manko-Novikov black hole with $a = 0.98, q = 2$. The red, green and blue lines on the background are drawn. They are drawn at a lower radius of $r = 6M$ to allow for a more zoomed image. Each image has 9 orbits, the central orbit is given by the pixel indicated on the bottom right of the image, while the 8 around it are each offset along the image by a fraction of a pixel.
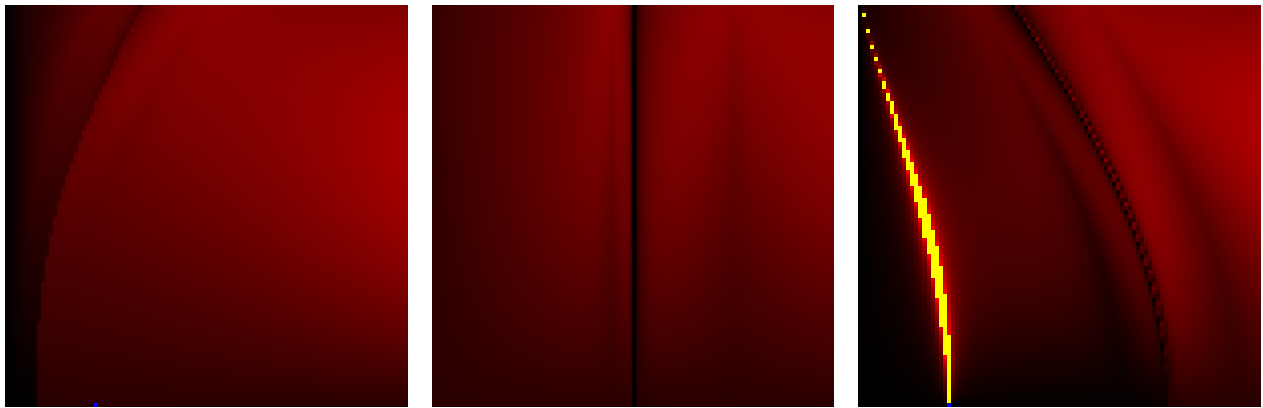
(a) A Kerr black hole with $a = 0.98M$, orbits are prograde to spin.

(b) A Kerr black hole with $a = 0M$, or a Schwarzschild black hole.

(c) A Kerr black hole with $a = 0.98M$, orbits are retrograde to spin.

Figure 15: Low radius orbits in the Kerr spacetime. Orbits are left to run for one rotation, that is to say from $\phi = 0$ to $\phi = 2\pi$. Black gives small deviation from starting positions in r, θ, p_r, p_θ. Red gives larger deviation, yellow gives off-scale deviation.
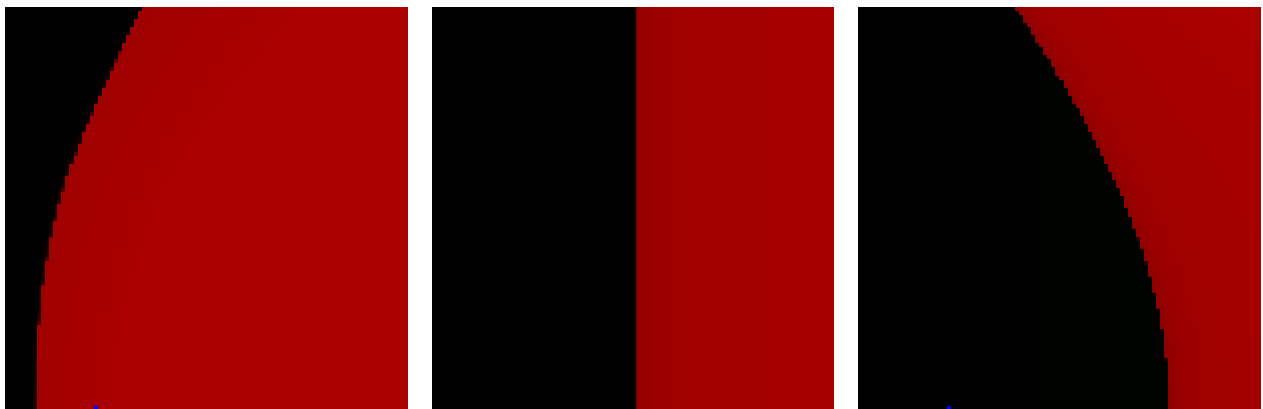
(a) A Kerr black hole with $a = 0.98M$, orbits are prograde to spin.

(b) A Kerr black hole with $a = 0M$, or a Schwarzschild black hole.

(c) A Kerr black hole with $a = 0.98M$, orbits are retrograde to spin.

Figure 16: Low radius orbits in the Kerr spacetime. Orbits are left to run for one rotation, that is to say from $\phi = 0$ to $\phi = 2\pi$. Orbits at black pixels fall into the black hole, while orbits at red pixels fly off to infinity. The orbits at the edge between the two regions are (pseudo)-periodic.
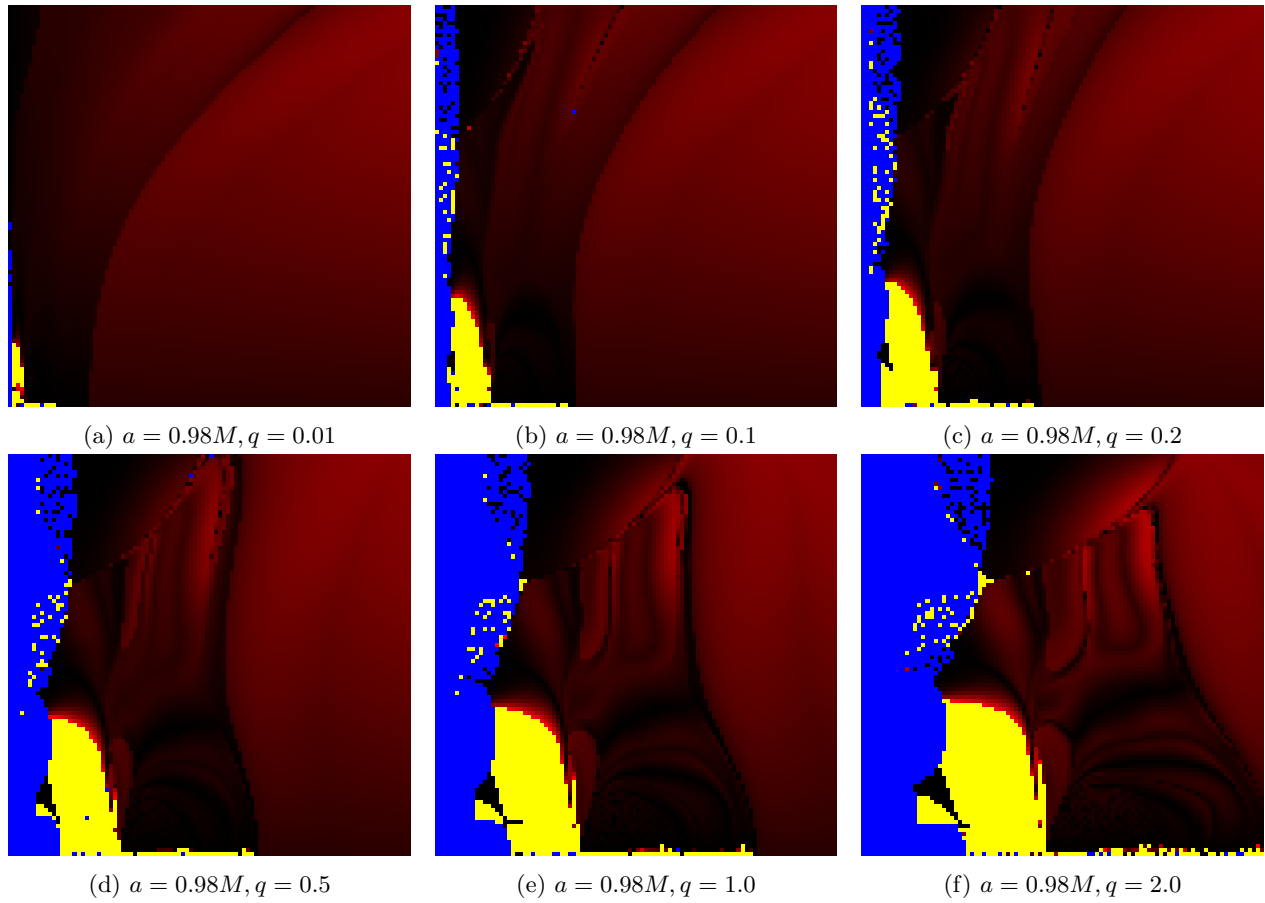
(a) $a = 0.98M, q = 0.01$ (b) $a = 0.98M, q = 0.1$ (c) $a = 0.98M, q = 0.2$

(d) $a = 0.98M, q = 0.5$ (e) $a = 0.98M, q = 1.0$ (f) $a = 0.98M, q = 2.0$

Figure 17: Low radius orbits in the Manko Novikov spacetime. Again red is high deviation from the start after one rotation in ϕ, black is low deviation. Here blue means a calculation error, due to division by zero when reaching the horizon.

(a) $a = 0.98M, q = 0.01$ (b) $a = 0.98M, q = 0.1$ (c) $a = 0.98M, q = 0.2$

(d) $a = 0.98M, q = 0.5$ (e) $a = 0.98M, q = 1.0$ (f) $a = 0.98M, q = 2.0$
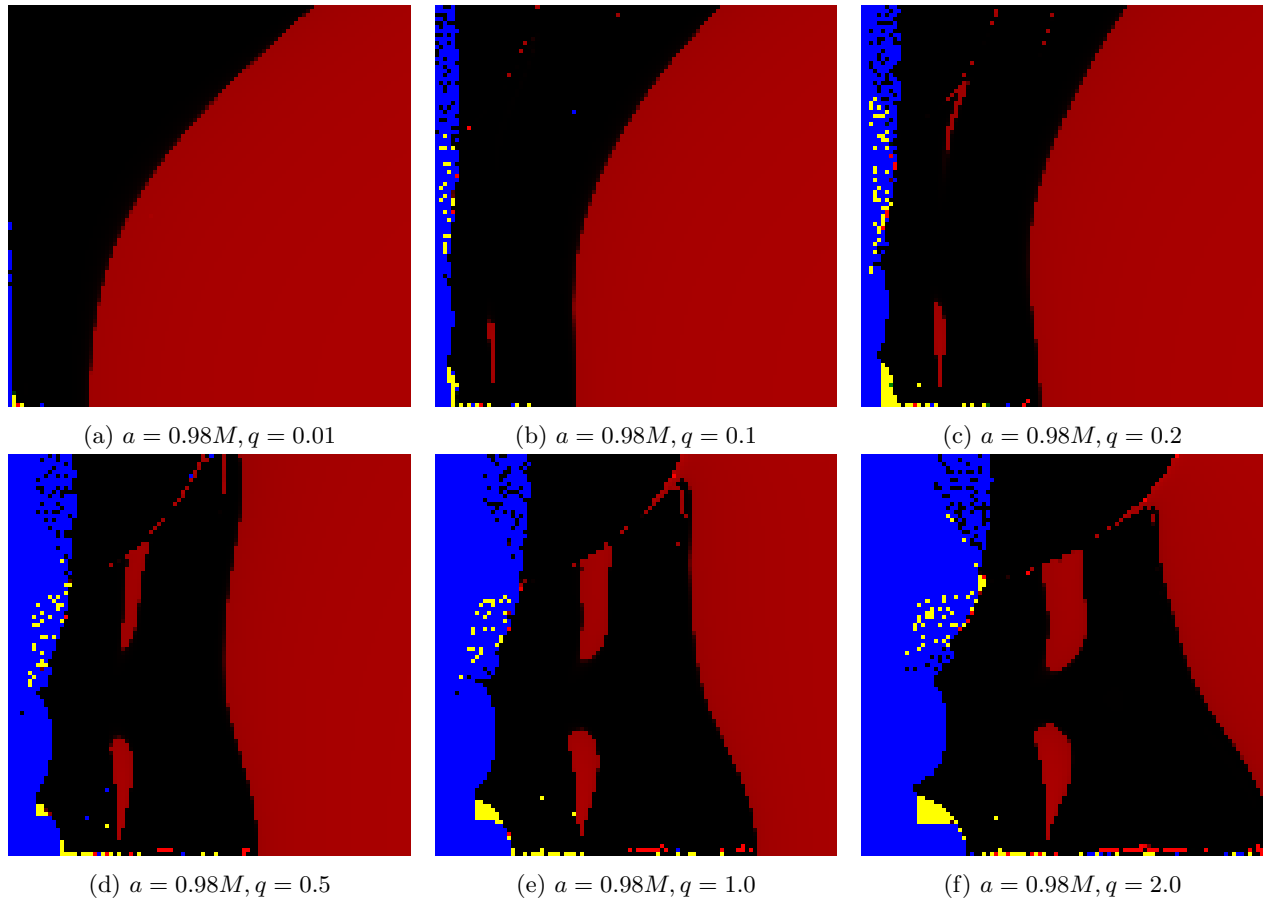
Figure 18: Low radius orbits in the Manko Novikov spacetime. Again red means the orbits escape, black means they fall in, yellow and blue means unexpected coordinates (eg $r < 0$ or NaN) due to calculation errors.

Figure 19: Low radius orbits of a Manko Novikov spacetime with $a = 0.98M, q = 2.0$. Black pixels fall into the event horizon while red pixels leave. Blue and yellow pixels stand for calculation errors. Dark red pixels means the pixels take multiple rotations to leave the bounded region.
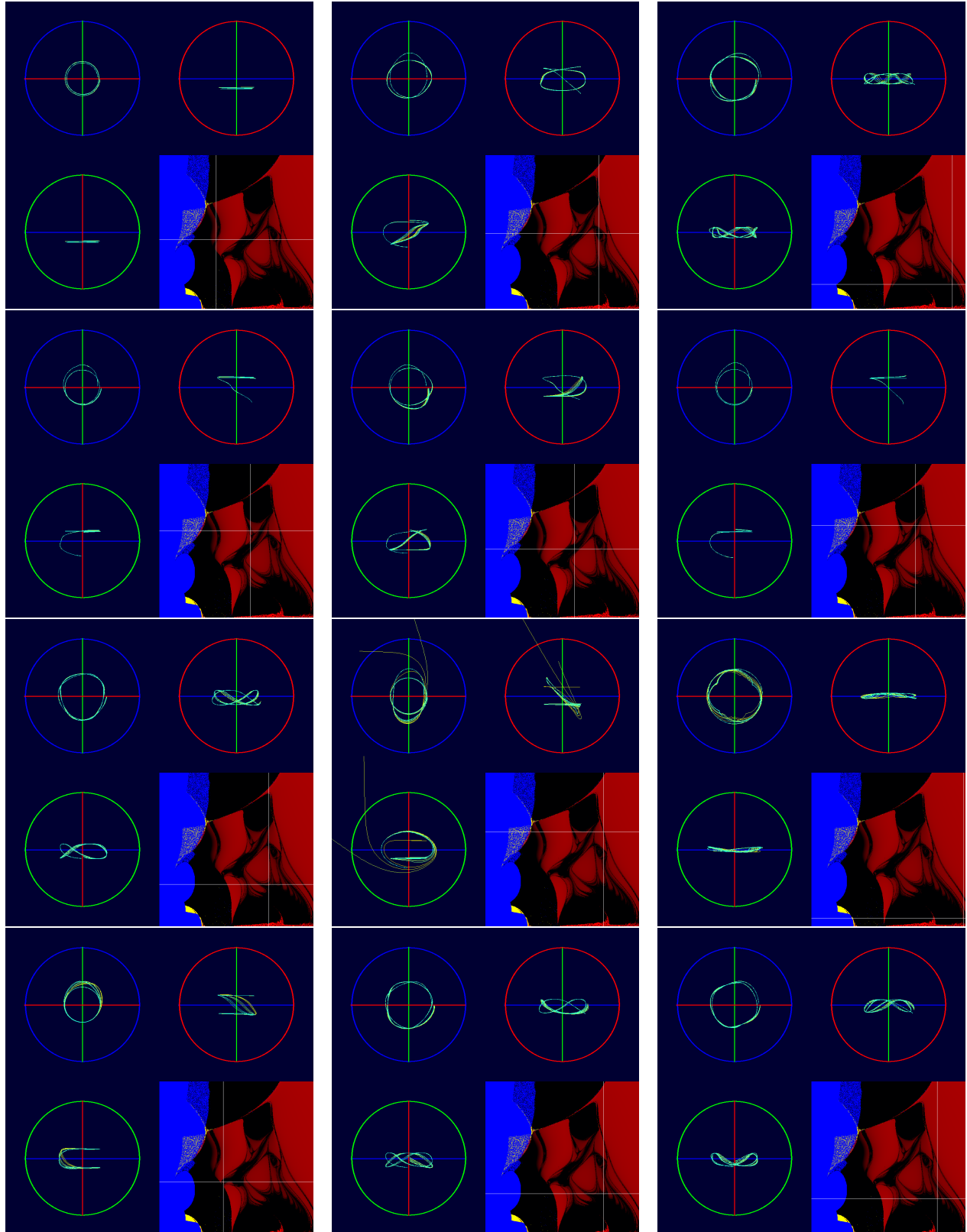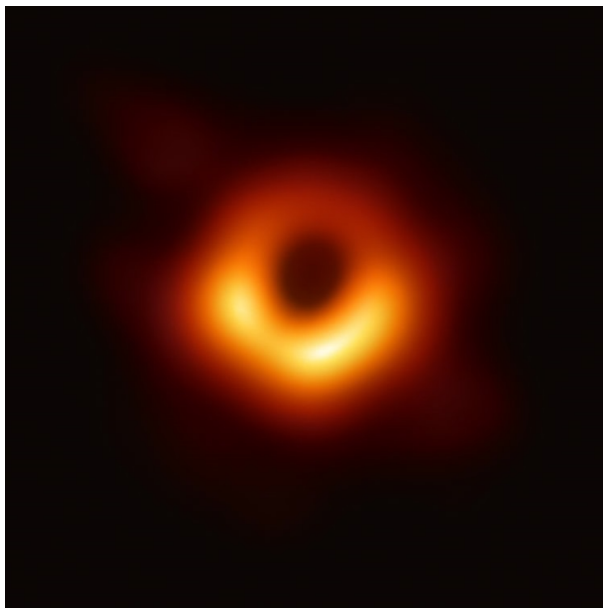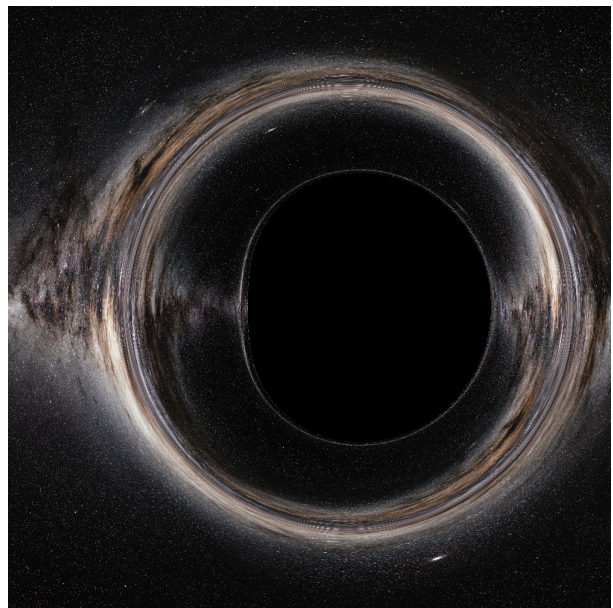
Figure 20: Low radius orbits in the Manko Novikov spacetime with $a = 0.98, q = 2$. Three perspectives are shown, the red, green and blue circles indicate the perspectives.

(a) The visual observation of a black hole in Messier 87 made by the Event Horizon Telescope [al19].

(b) A Kerr black hole with $M = 0.5, S = 0.98M^2$ simulated.

Figure 21: Side by side: the image of a black hole by the Event Horizon telescope and a simulation of the visual signature of a Kerr black hole.

References

[Aki+19] Kazunori Akiyama et al. "First M87 Event Horizon Telescope Results. VI. The Shadow and Mass of the Central Black Hole". In: *Astrophys. J. Lett.* 875.1 (2019), p. L6. DOI: 10.3847/2041-8213/ab1141. arXiv: 1906.11243 [astro-ph.GA].

[al19] Event Horizon Collaboration et al. "First M87 Event Horizon Telescope Results. I. The Shadow of the Supermassive Black Hole". In: *ApJL* 875 (2019). https://eventhorizontelescope.org/.

[Bri08] Jeandrew Brink. "Spacetime Encodings II - Pictures of Integrability". In: *Physical Review D* 78 (Aug. 2008). DOI: 10.1103/PHYSREVD.78.102002.

[Bru] S. Brunier. *The Milky Way Panorama.* https://www.eso.org/public/netherlands/images/eso0932a/.

[CF 16] A. Oancea C.F. Paganini B. Ruba. "Characterisation of null geodesics on Kerr spacetimes". In: (2016). URL: https://arxiv.org/abs/1611.06927.

[Car19] S.M. Carroll. *Spacetime and Geometry.* Cambridge University Press, 2019. ISBN: 9781108488396.

[D M98] D. Salamon D. McDuff. *Introduction to Symplectic Topology.* Clarendon Press, Oxford, 1998. ISBN: 0198504519.

[Ghe+98] A. Ghez et al. "High Proper Motion Stars in the Vicinity of Sgr A*: Evidence for a Supermassive Black Hole at the Center of Our Galaxy". In: *Astrophysical Journal* 509 (July 1998). DOI: 10.1086/306528.

[GA23] Sushant G. Ghosh and Misba Afrin. "Shadows of hairy Kerr black holes and constraints from M87*". In: *16th Marcel Grossmann Meeting on Recent Developments in Theoretical and Experimental General Relativity, Astrophysics and Relativistic Field Theories.* Jan. 2023. DOI: 10.1142/9789811269776_0093.

[Hai10] Ernst Hairer, ed. *Lecture notes: Geometric Numerical Integration.* 2010. URL: https://www.unige.ch/~hairer/poly_geoint/week2.pdf.

[Hos] Victoria Hoskins, ed. *Symplectic Quotients: Moment Maps, Symplectic Reduction and the Marsden-Weinstein-Meyer theorem.* https://userpage.fu-berlin.de/hoskins/Sympl_reduction.pdf.

[Ker63] R. P. Kerr. "1Gravitational Field of a Spinning Mass as an Example of Algebraically Special Metrics". In: *Phys. Rev. Lett.* (1963).

[Lee13] J.M. Lee. *Introduction to Smooth Manifolds, Second Edition.* Springer Science+Business Media, 2013. ISBN: 9781441999818.

[Lev16] T. Levi-Civita. "Nozione di parallelismo in una varietà qualunque [The notion of parallelism on any manifold]." In: *Rendiconti del Circolo Matematico di Palermo* 42 (1916).

[M W18] J. Jing M. Wang S. Chen. "Chaotic shadow of a non-Kerr rotating compact object with quadrupole mass moment". In: *Phys. Rev.* (2018). https://arxiv.org/abs/1801.02118.

[MN92] V. S. Manko and I. D. Novikov. "Generalizations of the Kerr and Kerr-Newman metrics possessing an arbitrary set of mass-multipole moments". In: *Class. Quantum Grav.* 9 (1992).

[R S91] E. Lerman R. Sjamaar. "Stratified Symplectic Spaces and Reduction". In: *Annals of Mathematics* (1991).

[Sch16] K. Schwarzschild. "Über das Gravitationsfeld eines Massenpunktes nach der Einsteinschen Theorie". In: *Sitzungsberichte der Königlich Preussischen Akademie der Wissenschaften* 7 (1916). https://arxiv.org/abs/physics/9905030 (Translation by S. Antoci and A. Loinger).

[Zil21] Fabian Ziltener, ed. *Lecture Notes Symplectic Geometry.* 2021.